ABSTRACT

Title of thesis: BIOLOGICALLY INSPIRED NAVIGATIONAL STRATEGIES USING ATMOSPHERIC SCATTERING PATTERNS

Julia R. Ashkanazy, Master of Science, 2015

Thesis directed by: Professor J. Sean Humbert
Department of Aerospace Engineering

A source of accurate and reliable heading is vital for the navigation of autonomous systems such as micro-air vehicles (MAVs). It is desirous that a passive computationally efficient measure of heading is available even when magnetic heading is not. To confront this scenario, a biologically inspired methodology to determine heading based on atmospheric scattering patterns is proposed. A simplified model of the atmosphere is presented, and a hardware analog to the insect Dorsal Rim Area (DRA) photodetection is introduced. Several algorithms are developed to map the patterns of polarized and unpolarized celestial light to heading relative to the sun. Temporal information is used to determine current solar position, and then merged with solar relative heading resulting in absolute heading. Simulation and outdoor experimentation are used to validate the proposed heading determination methodology. Celestial heading measurements are shown to provide closed loop heading control of a ground based robot.

BIOLOGICALLY INSPIRED NAVIGATIONAL STRATEGIES USING ATMOSPHERIC SCATTERING PATTERNS

by

Julia R. Ashkanazy

Thesis submitted to the Faculty of the Graduate School of the
University of Maryland, College Park in partial fulfillment
of the requirements for the degree of
Master of Science
2015

Advisory Committee:
Professor J. Sean Humbert, Chair/Advisor
Professor Inderjit Chopra
Professor Robert M. Sanner

Acknowledgments

First I would like to thank Dr. Sean Humbert for granting me the opportunity to work and grow at the Autonomous Vehicle Lab, and for seeing potential in the overenthusiastic freshman that knocked at his door one winter afternoon in 2007. The experiences and support provided by the AVL have been invaluable.

I would also like to thank the University of Maryland faculty. Thank you as well to Dr. Sanner and Dr. Chopra for agreeing to be part of my committee.

Next I would like to especially thank all present and past members of the AVL. You were always there for me to answer questions and bounce ideas off of. I learned a lot from all of you. It might be cliche, but I am in earnest when I say that I wouldn't have made it this far without you guys.

Hector Escobar, thank you so much for all of your extended help with serial communications and Vicon. All of those packets and words almost make some sort of sense to me now. Thanks for always being there and helping me through when things just weren't quite working.

Badri Ranganathan, solicited or otherwise, I really appreciated all of your advice. You always knew how steer me back on track whenever I started to veer on a research tangent. I also really enjoyed having comparative language and cultural discussions with you.

Andrew Kehlenbeck, thanks for nearly electrocuting yourself to help me figure out which lead was ground and which was power. I also appreciate you letting me borrow your your microquad screws. Thanks for always taking my random questions

seriously and giving me an introduction to quaternions.

Greg Gremillion, thank you so much for all of your help and suggestions over the years. Thank you as well for enlightening me on some critical truths, such as the difference between a grilling and barbecuing.

Lina Castano, thank you for coming out in the bitter freezing weather to help test the ground robot, for Taylor time, and for always being there to lend a supportive and helping hand.

To Joseph Conroy, thank you for all of your continued guidance since my freshman days at the AVL.

On that note, I suppose I should express my gratitude to peanuts, unsweetened chocolate, and protein pasta for being the source of my vitality. Yum! And of course Beethoven, Metallica, Idan Raichel, and Eminem, thank you guys for keeping the rhythm alive and allowing me to complete this thesis.

Finally I would like to thank my family, and most especially my mother and father without whom I literally would not be here. Thank you Mom and Dad for loving me and supporting me during rough times and happy times, and through all of my decisions no matter how off the beaten path they might be.

Contents

List of Figures

List of Abbreviations

Nomenclature

α	Angle of polarization
β_m	Scattering angle independent scattering coefficient
$\beta_m(\gamma)$	Scattering angle dependent scattering coefficient
χ	Filter orientation, CW relative to top of image plane, deg
χ_{max}	Filter orientation resulting in maximum intensity, deg
Δ_2	Angular offset between desired and actual camera filter 2 orientation
$\Delta_{2/1}$	Angular distance between camera 1 and 2 filter orientations
$\Delta_{3/2}$	Angular distance between camera 2 and 3 filter orientations
ℓ	Image side length, pixels
γ	Scattering angle
λ	Wavelength
ψ	Azimuth angle
ψ_m	Motor angle from origin
ψ_s	Solar azimuth angle
$\psi_{a/s}$	Solar/anti-solar azimuth angle, modulo 180°
θ	Elevation angle
ζ	Zenith angle
d	Degree of polarization
E	Irradiance
E_0	Irradiance of solar energy from the top of the atmosphere
I	Intensity
N	Number of particles
n	Refractive index
Z_0'	SL reduced height

Chapter 1: Introduction

Autonomous Unmanned Air Vehicles (UAVs) are capable of executing a large and diverse array of tasks, both military and civilian. UAVs have been used and are being developed for applications including military intelligence reconnaissance and surveillance (ISR), hazardous chemical detection, disaster relief, commercial delivery service, and farming. Much of recent research has focused on developing Micro Air Vehicles (MAVs), small UAVs designed to nimbly negotiate cluttered environments at low altitudes while remaining relatively covert.

A reliable navigation system is vital to the success of a UAV mission. Finding a suitable method for UAV navigation is especially challenging for smaller UAVs such as MAVs which have a very limited payload capacity and are thereby constrained by computational power and weight. Additionally, MAVs often function around buildings where electromagnetic interference can disrupt magnetic based heading measurements. Furthermore, GPS frequently cannot, or is preferred not to be used. This means that common navigational strategies employing GPS and magnetic compass are not always appropriate solutions.

Several visual methods have been developed to assist UAV navigation in GPS denied scenarios including Simultaneous Localization and Mapping (SLAM), optic

flow, and path integration techniques. SLAM is a very useful technique for getting complete situational awareness of a limited area, however it is rather computationally cumbersome, and is prone to accumulation in position estimation errors without some sort of loop closure method. Optic flow has proven to be a very computationally light obstacle avoidance tool, however optic flow is a relative measure and requires fusion with additional sensors to provide more useful distance or heading measurements. Path integration is the name given to the type of dead reckoning methods that animals are thought to use for navigation. However, all dead reckoning methods are prone to error accumulation over time without a way to accurately measure heading or distance.

It is supposed that many of nature's MAVs, including insects [1] [2] [3], birds [4], fish [5] [6], and even bats [7], are able to overcome these navigational challenges by making use of the predictable pattern of atmospherically scattered light. These celestial cues are used to determine solar relative heading. Insects, equipped with an internal clock in the form of circadian rhythm [8] [9], are able to locate where the sun should be at any given time of the day. Absolute heading is then resolved by summing solar azimuth with current heading relative to the sun.

The objective of this thesis is to develop and compare strategies for utilizing atmospheric scattering patterns for navigation based on biological principals. These methods are developed in a simulation environment, and then analyzed through outdoor testing. Autonomous real time heading control, using atmospheric heading determination methods, is then demonstrated on a ground based robot and through simulation of a quadrotor.

1.1 Celestial Navigation in Nature

In the mid 1940's, Karl von Frisch noticed that after a single honeybee leaves a feeding ground, a swarm of bees often returns to feed at that same location [10]. This observation instigated several questions. Did the initial honeybee somehow communicate the whereabouts of the food to his companions? If so, how was this information encoded? Several studies have led to the conclusion that honeybees are able to disclose the location of a food source to the rest of the hive by performing a "waggle dance [11]".

The dance codes a vector including the *current* heading angle relative to the sun and the amount of energy, as a function of wind conditions, needed to get to the desired destination. The angle of the dance changes over the course of the day indicating that honeybees keep track of solar position changes. Successful communication was shown to rely on the bees' ability to see a small portion of blue sky from the hive. The sun itself did not need to be seen [12]. It was thus concluded that honeybee navigational cues are based on atmospheric scattering patterns [13] [14], specifically relying on the angle of polarization.

Behaviors, indicating the use of atmospheric scattering patterns, have been observed in several other species including crickets [15], birds [4], bats [7], desert ants [16], and the migrating desert locust [17]. Monarch butterflies have also been shown to rely on celestial cues for navigation [18] [19]. However, while monarch butterflies are sensitive to polarized light, they primarily rely on the sun itself as a celestial navigational cue [20].

The anatomical origin for polarization vision in insects is the Dorsal Rim Area (DRA) of the compound eye [21]. Insects who employ atmospheric scattering patterns possess a uniquely structured DRA where Microvilli of each rhabdomere are arranged in linear rows. The majority of rhabdomers within an ommatidium have microvilli oriented in a single primary direction, while the remaining rhabdomers have microvilli oriented in a secondary orientation perpendicular to this primary direction. The primary directions of ommatidia are arranged in a fan-like pattern across the DRA [22]. In this way, the highly structured monochromatic photodetectors of the DRA essentially act as a wide field array of linear polarizing filters. It is supposed by many that the signals from the secondary perpendicular direction are subtracted from the primary signals thereby feeding through only the polarized component of the light, or the second Stokes parameter. This is known as polarization opponency. Across species, the wavelength of peak sensitivity for these photodetectors is in the blue to UV range. This is likely due to the fact that the atmospheric scattering pattern of smaller wavelength light is less affected by clouds.

Photodetection in the DRA is the initial stage in a polarization sensitive (POL) sensory-motor pathway that resolves spatial celestial cues into yaw commands. Polarization sensitive neurons are easily distinguishable from other neurons since they respond sinusoidally to angle of polarization. From the DRA, polarization information passes into the Optic Lobe (OL) consisting of the Lamina and the Medulla. Extensive research has been performed here on what have been termed he POL1 neurons in crickets [21]. Three "types" of POL1 neurons have been found in each compound eye of the cricket [23], each type with a different polarization tuning angle

at approximately 10°, 60°, and 130°. However, since there is currently no evidence that these POL1 neurons connect to the central complex [24], it is uncertain what the function of these neurons are.

Additional inputs to this pathway include temporal information extracted from circadian rhythm [8], and non-polarized light information. Circadian rhythm information allows the insect to compensate for changes in the pattern of atmospheric scattering due to the migration of the solar azimuth throughout the day. As the pattern of polarized light can be nearly symmetric, the patterns of *un*polarized light can allow an insect to distinguish between the solar and anti-solar hemispheres. It is possible that some insects recognize the solar hemisphere as the region in the sky possessing the greatest overall intensity. Evidence suggests that the desert locust can identify the anti-solar hemisphere by its higher concentration of short wavelength light, and the solar hemisphere by its higher concentration of larger wavelength light [25]. Temporal and chromatic information are integrated with polarization signals from both eyes in the Anterior Optic Tubercle (AUTu) [26].

Processing of the signals from the polarization pathway into compass direction takes place in the Central Complex (CC) [27]. Here, there are highly organized arrays and stacks [28] of neurons which possibly correspond to a "maplike representation of the sky [29]." Evidence suggests that the CC is the location of the internal "sun compass" of the insect [30]. It is possible that the stacks of the protocerebral bridge code for different e-vectors, and population coding is used to resolve the responses from the neuron stacks into a single e-vector. Compass signals from the CC are then sent down the descending motor pathways to produce yaw responses [31].

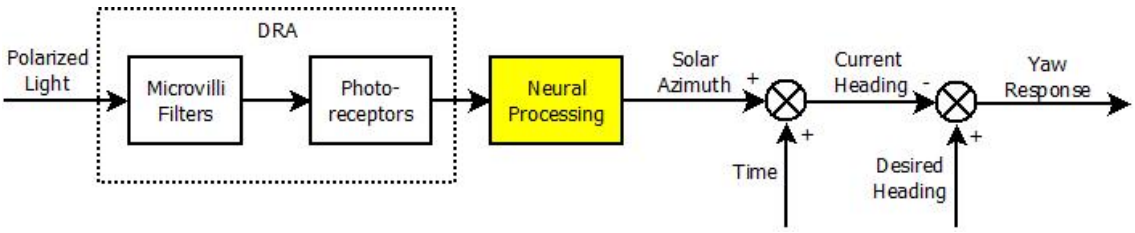

Figure 1.1: Flow diagram model of resolution of polarized light into yaw response

Sakura et al. [32] propose a neural network model of how the resolution of POL1 neuron signals is increased over several stages of neurons, and how the CC resolves a single e-vector from this information. An electrophysiological study is performed to support their claim that some form of population code is used to represent e-vector direction in the CC.

1.2 Detecting Atmospheric Scattering Patterns

The idea of employing atmospheric scattering patterns for navigation is not new. Vikings [33] who sailed near the North Pole where earth's magnetic poles are hard to detect, are said to have used a "sunstone", which essentially acted as a linear polarizing filter, for a compass. The "solar compass" was developed in 1851 to allow surveyors and minors to find true north from the sun when surrounding iron deposits interfered with magnetic north. Early pilots who flew around the north pole adapted similar compasses. A "sky compass" based on polarized light patterns was developed in 1954 to allow field geologists to get their bearing when the sun was not in the line of sight [34].

In order to understand what navigational cues are used by desert ants, Horvath and Wehner [35] performed the first "wide-field, video-polarimetric study of skylight polarization." This revealed that day to day changes in degree of polarization are much more prominent than changes in angle of polarization. The results of this study are consistent with biological findings that polarization sensitive neurons primarily respond to changes in angle of polarization rather than degree of polarization [32]. Further investigation by Pomozi et al. [36] led to a potential resolution of the UV paradox[1]. They suggested that insects' DRA ommatidia are tuned to light in the UV wavelength since polarization patterns are best preserved through clouds for smaller wavelength rays.

Based on biological observations, Lambrinos et al. [37] [38] developed a method for ground robot navigation based on polarization patterns. This method analytically solves for the angle of polarization based on modeled log-amplified inputs from 3 POL-OP units each consisting of 2 POL-sensors. Ambient light sensors were used to resolve solar/anti-solar ambiguity. Results show successful completion of both 15 and 30 segment trajectories, and demonstrate feasibility of a polarization based method for ground robot navigation.

Chu et al. [39] [40] [40] implemented the methodology developed by Lambrinos on a microcontroller, and systematically investigated polarization sensor accuracy through various controlled indoor calibrations. Zhao et al. [41] further improve upon this methodology by using a piecewise definition of the atan function, thereby

[1]The UV paradox questions why insect DRA ommatidia are tuned to UV light while longer wavelengths of light in the sky provide higher intensity and degree of polarization

preventing undefined solutions and forcing results into the correct quadrant. Higashi et al. [42] proposed a simplified version of the sensor model by eliminating the polarization opponent crossed analyzers.

The polarization sensors used in the methods discussed above rely on point measurements and are therefore prone to error from obstructions such as birds and clouds. Wider field methodologies have been employed that have the potential to mitigate these issues to some degree. Wang et al. [43] proposed a multi-camera solution which greatly increases field of view, but is rather bulky. Sarkar et al. [44] developed a compact CMOS polarization sensor. Both of these methods utilize Stokes parameters for measurements and require polarization filters angles of 0, 45, and 90 degrees. Stokes parameter methods require calculating the angle and degree of polarization. As discussed above, biological systems likely do not rely heavily degree of polarization for navigation. Consequently these methods require a look up table or continuous calibration since degree of polarization and atmospheric intensity vary over the course of the day. Successful control of a vehicle using either of these methods is yet to be shown.

1.3 Thesis Contributions and Organization

Thus far, only a handful of methods have been proposed and developed for determining relative solar azimuth from atmospheric scattering patterns. In this thesis, several new algorithms are presented for celestial based navigation. A purely linear computational approach is also provided for more straightforward implemen-

tation in an analogue sensor framework. The algorithms are introduced for a low cost, off the shelf, three camera based hardware configuration, but can readily be generalized to various single and multi-camera configurations and polarization filter directions. Cameras are chosen over photodiodes to increase field of view, thereby reducing measurement error due to visual disturbances. Cameras also allow the spatial pattern of atmospheric pattern to be utilized. Simulation and experimental results are used to analyze and compare the various methods. It is then demonstrated how celestial based heading can be used for reliable closed loop heading control.

Chapter 2 introduces a model of polarized light and atmospheric scattering. This model is used to generate a simulation environment, and to motivate algorithm development and sensor design. Chapter 3 proposes several algorithms for determining the relative azimuth of the sun based on the patterns of polarized and unpolarized atmospheric radiation. In Chapter 4 these methods are analyzed and compared using simulation and experimental results. Chapter 5 then provides an implementation of the sensing methodology for control of a ground based differential wheeled robot. Further, a simulation of closed loop control of a quadrotor is presented. A discussion of conclusions and future work is provided in Chapter 6.

Chapter 2: Model and Simulation of Atmospheric Scattering

The optical principles behind transmittance of light through a medium such as the atmosphere are rather complex. In order to gain a practical understanding of the polarization and intensity distributions observed in the sky, assumptions and simplifications need to be made. This chapter first presents a Rayleigh scattering based model of the atmosphere. Then a model of how a set of idealized zenith facing cameras, fitted with linear polarizing filters, might perceive the sky, is introduced.

2.1 What is Polarized Light?

A light wave's motion can be described by its direction of propagation and oscillatory behavior. The direction of light propagation is a radial line from the source of light. Oscillatory behavior is divided into two categories: linear and circular. Circular oscillation is characterized by tangential looping motion perpendicular to the direction of propagation. Circular oscillations in time can be visualized as spirals about the axis of propagation. Linear oscillation is characterized by radial back and forth motions perpendicular to the direction of propagation. One can picture these linear oscillations in time as sinusoidal waves rotated about the axis of propagation. Atmospherically scattered light is dominated by linear oscillations. Therefore the

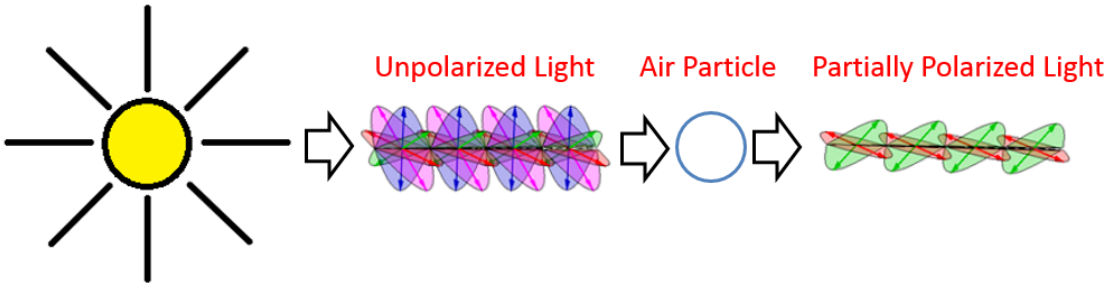

Figure 2.1: Scattering of light by atmospheric air particle

remainder of this discussion will be restrained to linear polarization.

A light wave that oscillates in all possible directions perpendicular to the direction of propagation is called *unpolarized* light. Light in a vacuum will remain unpolarized. However, when light travels through a medium, it is possible that some of its directions of oscillation are impeded. When a light wave oscillates in only one direction it is called *polarized light*, and when a light wave oscillates in more than one direction it is called *partially-polarized* light. If light is prevented from oscillating in all directions, it will not pass through the medium.

Light waves propagate radially from the sun, and oscillate in all directions perpendicular to the direction of propagation. However, upon reaching the earth's atmosphere, these light waves are refracted and reflected by air particles resulting in oscillation in only a limited number of directions. Thus atmospherically scattered light is partially polarized. The primary direction of oscillation is termed the *angle of polarization*, α. The ratio of the wave oscillating in this primary direction to the wave not oscillating in this primary direction is called the *degree of polarization*, p.

A sky gazer will notice that these reflections and refraction of sunlight do not

create a uniform intensity firmament. Rather, such an observer will see a sublime gradient of light and color. Bright ivory shades encircling the sun and horizon, gently fade into deep rich hues of periwinkle blue. This variation of sky intensities is caused by the distribution of air particles throughout the atmosphere. Air density decreases with increased elevation from the horizon to zenith, as does the average particle size. Light scattered by particles larger than or about the same size as the wavelength of light is generally modeled by Mie Scattering. The scattering of light by particles that are much smaller than the wavelength of light are modeled by Rayleigh scattering. Since the insect DRA is directed zenithally where air particles are generally much smaller than the wavelength of light, Rayleigh scattering is an appropriate model. Furthermore, Pomozi et al. [36] have shown that the Rayleigh single scattering model provides a very good approximation of the behavior of atmospheric scattering at higher elevations.

2.2 Geometry of Atmospheric Scattering

Before proceeding with a discussion of the principles of atmospheric scattering, a description of atmospheric geometry and notation is presented. We begin with a hemisphere of unit radius. The planar surface of this hemisphere is centered at the location of the observer, O, and is concentric with the horizon. O is the origin of an inertial North-East-Down (NED) coordinate system (see Appendix A), defined as $\mathcal{I}_{NED} = (O, \mathbf{e}_N, \mathbf{e}_E, \mathbf{e}_D)$. The location of any point on the hemisphere can be described by a rotation about $\mathcal{I}_{NED}$'s 3-axis, $\mathbf{e}_D$, followed by a rotation about an

intermediate frame's 2-axis. The resulting reference frame is the observer reference frame. The 1-axis of the observer frame will be along the direction of the point of interest.

The rotation about the 3-axis is the *azimuth angle*, $\psi \in (-180°, 180°]$, and the rotation about the 2-axis is the *elevation angle*, $\theta \in (-90°, 90°]$. Azimuth angle is measured from $\mathbf{e}_N$, and elevation angle is measured from the horizon. Positive rotations are defined as counterclockwise, while negative rotations are defined as clockwise. The *zenith*, Z, is the point located at an elevation angle of 90°. Zenith angle, $\zeta \in (-90°, 90°]$, is the angle along a meridian line between the Z and some point of interest. Otherwise stated,

$$\zeta = 90° - \theta. \tag{2.1}$$

Now suppose that this observer O is looking at some point in the sky, P, with coordinates (ψ_P, θ_P), while the sun, S, is located at (ψ_S, θ_S). The *scattering plane* is defined as the plane containing O, P, and S. Next, the *observation angle* γ is defined as the angular distance along the scattering plane between the observed point and the sun. The observation angle of an observed point with azimuth and zenith angles (ψ_p, ζ_p), given solar position (ψ_s, ζ_s), can be calculated via spherical trigonometry as follows.

$$\cos(\gamma) = \cos(\zeta_s)\cos(\zeta_p) + \sin(\zeta_s)\sin(\zeta_p)\cos(\psi_s - \psi_p) \tag{2.2}$$

The angle of polarization, α, as mentioned above, is the dominant angle of

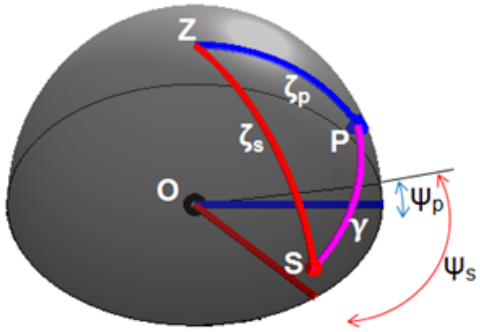

Figure 2.2: Geometry of Atmospheric Scattering

oscillation that a light wave exhibits. Relative to the observer located at O, the angle of polarization of incident sunlight is determined as follows. First a vector perpendicular to the scattering plane, $\mathbf{n}$, is determined. Letting $\mathbf{r}_{S/O}$ be the vector to S from O, and $\mathbf{r}_{P/O}$ be the vector to P from O,

$$\mathbf{n} = \mathbf{r}_{S/O} \times \mathbf{r}_{P/O}. \tag{2.3}$$

Next a vector, $\mathbf{m}$, tangent to the local meridian where the meridian intersects the scattering plane is found. The angle of polarization is defined as the angle from $\mathbf{m}$ to $\mathbf{n}$. The angle, θ, between any two vectors, $\mathbf{a}$ and $\mathbf{b}$, can be found using the geometric definition of the dot product.

$$\mathbf{a} \cdot \mathbf{b} = ||\mathbf{a}||\,||\mathbf{b}||\cos(\theta)$$

Therefore

$$\alpha = \cos^{-1}\left(\frac{\mathbf{m}\cdot\mathbf{n}}{||\mathbf{m}||\,||\mathbf{n}||}\right) \tag{2.4}$$

can be used to find the angle of polarization.

2.3 Rayleigh Scattering Based Model

Rayleigh scattering is the theory developed in the late 19th century by British physicist Lord Rayleigh. The theory describes the dispersion of electromagnetic radiation by particles with radius much smaller than the wavelength of the light waves being dispersed. The permanent gasses of earth's atmosphere are well described by the Rayleigh atmosphere. These permanent gases consist of approximately 78% nitrogen, 21% oxygen, and 1% trace gasses. Generally dry atmospheric air can be modeled as an ideal gas.

The law of Rayleigh scattering of electromagnetic energy through atmospheric permanent gases is based on five assumptions [45].

1. The scattering particles are much smaller than the wavelength of the light being scattered.

2. The scattering particles are non-ionized.

3. The index of refraction, n, of the particles is approximately 1.

4. The scattering particles are *isotropic*, or have no preferred oscillation direction when penetrated by light waves.

5. The resonance frequency of the scattering particle is not close to the light wave's frequency.

Following the works of McCartney [46] and Coulson [45], Rayleigh scattering principles are applied to quantify polarization and intensity throughout the sky. Using the Rayleigh single scattering model, it is assumed that scattering is performed by a small, spherical, isotropic particle. The prototypical air particle is modeled by the average properties, weighted by particle prevalence, of the atmosphere's permanent gases. Since photon energies are not changed during Rayleigh scattering, particle interaction is described by the lightly damped elastic model.

Monochromatic light with intensity $I(\gamma)$ will have intensity $I(\gamma) + dI(\gamma)$ after exiting a medium such as air. Introducing a volume scattering coefficient, $\beta_m(\gamma)$, the differential intensity change over path increment ds is

$$dI(\gamma) = \beta_m(\gamma) I(\gamma) ds \tag{2.5}$$

Now imagine a vertical column of unit cross section from the observer, O, to the top of the atmosphere. The ratio of the total mass of air in this column per cross sectional area, to the air density at sea level is called the *reduced height*, z'. When the observer is around sea level, the reduced sea level height, z'_0, can be used, where

$$Z'_0 = \frac{RT_0}{g} = 7.997 \times 10^3 \text{m}. \tag{2.6}$$

By assuming that the earth and its atmosphere are plane parallel, $ds = \sec(\zeta_P)$

along the path from observer to observed point. The irradiance of solar energy from the top of the atmosphere, E_0, will be reduced to irradiance

$$E = E_0 e^{-\beta_m z' \sec(\zeta_S)} \tag{2.7}$$

after traveling the distance z' to the observer, where β_m is the total scattering coefficient. Thus, (2.5) becomes

$$dI(\gamma) = E_0 e^{-\beta_m z' \sec(\zeta_S)} \beta(\gamma) \sec(\zeta_P) \tag{2.8}$$

where $I(\gamma) = B_m(\gamma)E$. Furthermore, the intensity will be attenuated by a factor of $e^{-\beta_m(z_0'-z')\sec(\zeta_P)}$ making the overall differential intensity change

$$dI(\gamma) = E_0 e^{-\beta_m z' \sec(\zeta_S)} e^{-\beta_m(z_0'-z')\sec(\zeta_P)} \beta(\gamma) \sec(\zeta_P) \tag{2.9}$$

Integrating (2.9), the intensity observed at a given observation angle is

$$I(\gamma) = \frac{E_0 \beta_m(\gamma)}{\beta_m} \left[\frac{-e^{-\beta_m Z_0' \sec(\zeta_s)} - e^{-\beta_m Z_0' \sec(\zeta_p)}}{1 - \sec(\zeta_s)\cos(\zeta_p)} \right]. \tag{2.10}$$

The scattering coefficients in (2.10) are derived from electromagnetic theory of dipole interaction, using the assumptions of Rayleigh scattering listed above. A discussion of scattering performed by a model elemental scatter on an electromagnetic wave, as well as derivations for scattering constants, can be found in McCartney's "Optics of the Atmosphere [46]." The volume scattering coefficient of a molecule is

found to be

$$\beta_m = \frac{8\pi^3(n^2-1)^2}{3N\lambda^4}. \tag{2.11}$$

The total scattering coefficient, which describes "the ratio of flux completely scattered in all directions, by a unit volume of gas, to the irradiance of the incident light" is

$$\beta_m(\gamma) = \frac{\pi^2(n^2-1)^2}{2N\lambda^4}(1+\cos^2(\gamma)). \tag{2.12}$$

One can observe that the total scattering coefficient (2.12) can be solved for in terms of the volume scattering coefficient (2.11) as

$$\beta_m(\gamma) = \frac{3}{16\pi}\beta_m(1+\cos^2(\gamma)). \tag{2.13}$$

By substituting (2.13) into (2.10), an estimate of observed atmospheric intensity at observation angle, γ is

$$I(\gamma) = \frac{3}{16\pi}E_0(1+\cos^2(\gamma))\left[\frac{-e^{-\beta_m Z_0' \sec(\zeta_s)} - e^{-\beta_m Z_0' \sec(\zeta_p)}}{1-\sec(\zeta_s)\cos(\zeta_p)}\right]. \tag{2.14}$$

It was mentioned earlier that the degree of polarization is the ratio of the light wave oscillating in the primary direction to the wave not oscillating in this primary direction. Letting $I_\perp(\gamma)$ be the intensity of the polarized light wave vibrating perpendicular to scattering plane, and $I_\parallel(\gamma)$ be the intensity of the polarized light wave vibrating parallel to the scattering plane, the degree of polarization can be defined

as

$$p = \frac{I_{\perp}(\gamma) - I_{\parallel}(\gamma)}{I_{\perp}(\gamma) + I_{\parallel}(\gamma)}. \tag{2.15}$$

For small isotropic molecules, it is found that $I_{\perp}(\gamma)$ remains constant for all values of γ while $I_{\parallel}(\gamma)$ is proportional to $\cos^2(\gamma)$. Thus, for these conditions the degree of polarization becomes

$$p = p_{max} \frac{\sin^2(\gamma)}{1 + \cos^2(\gamma)} \tag{2.16}$$

where p_{max} is the maximum atmospheric degree of polarization.

2.4 Sensor Model

The previous section presented expressions for determining atmospheric intensity and polarization parameters at any given location in the sky. These values can now be used to estimate the intensity, $I_{\chi}(\gamma)$, that a camera fitted with a linear polarizing filter at a given orientation, χ, might detect. This observed intensity should be a sum of the polarized and non-polarized components of light.

$$I(\gamma) = I_{unpolarized}(\gamma) + I_{polarized}(\gamma) \tag{2.17}$$

Since p represents the fraction of light that is polarized, $1 - p$ represents the portion of light that is not polarized. The intensity of the unpolarized light viewed through a polarizing filter should be directly proportional to the total ambient in-

tensity.

$$I_{unpolarized}(\gamma) = (1-p)I(\gamma) \tag{2.18}$$

The observed intensity of polarized light on the other hand, is also a function of filter angle. Malus's law can be used to describe what happens to polarized light of initial intensity, I_0, that travels through two linear polarizing filters.

$$I = I_0 \cos^2(\Delta\chi) \tag{2.19}$$

In (2.19), $\Delta\chi$ is the angle between the axes of the two polarizers. From this one can see that the full initial intensity will be transmitted when the two polarizers are oriented parallelly, and the light will be fully extinguished when the two polarizers are oriented perpendicularly. It is also important to note here that Malus's law is 2π-periodic. The maximal intensity of atmospherically polarized light will be observed when the filter angle is aligned with the angle of polarization, and the minimal intensity will be observed when the filter angle and angle of polarization are perpendicular.

As discussed earlier, the angle of polarization is measured with respect to the intersection of the local meridian with the scattering plane, and is therefore measured in the observer frame $\mathcal{C}$. However, the filter angle is measured with respect to the vertical axis of the camera's image plane in the body frame $\mathcal{B}$, as described in Appendix A. The azimuthal rotation between the $\mathcal{B}$ and $\mathcal{C}$ reference frames is ψ_c. Consequently the angular distance between the polarization axis of the filter and

the observer's meridian is $\psi_c - \chi$, and the angular distance between the observed angle of polarization and filter angle is $\alpha - (\psi_c - \chi)$.

Combining the effects of Malus's law (2.19) with the above, the following expression can be used to describe the intensity of polarized light at a given observation angle.

$$I_{polarized}(\gamma) = pI(\gamma)\cos^2(\alpha - (\psi_c - \chi)) \tag{2.20}$$

Consequently, the intensity observed at observation angle, γ, through a polarization filter at angle, χ is

$$I_\chi(\gamma) = (1-p)I(\gamma) + pI(\gamma)\cos^2(\alpha - (\psi_c - \chi)). \tag{2.21}$$

2.5 Creating a Simulation

The goal of the simulation is to model the intensity patterns picked up by the 3 camera sensory system. The resulting simulated images can then be fed into the atmospheric scattering based heading algorithms in order to analyze and compare methodologies. The method presented can be used for simulating camera images on a ground based vehicle or a low flying MAV.

We start out by defining an image plane. It is assumed that all three cameras are identical and planarly mounted very close to each other. It is further assumed that all pixels are square and of the same size. Since the distance to points of interest in the sky are much greater than the distances between the cameras, it can

be assumed that all three cameras will observe identical images without polarization filters. Additionally, since generally the principal point of the image is close to the center of the image, it can also be assumed that the center pixel of the image is viewing the zenith when the camera image planes are parallel with the horizon.

The observable atmosphere can be modeled as a sphere of "large" radius centered at the robot or observer. This allows for the assumption that the distance from the observer to an observed point in the atmosphere is the same for any observed point. It should be noted that this model is unrealistic, but nonetheless very useful.

One might realize that the radius of the earth is about 2 orders of magnitude larger than the distance from the surface of the earth to the stratosphere. This implies that the distance from the observer to the sky would increase with decreasing observer elevation. However, the effect of keeping the distance to the sky constant is a radial distortion centered at the image principle point. Since this distortion is radially symmetric it should have little effect on determining heading, which is radially symmetric about the same axis. Furthermore, since fisheye lenses are being attached to the cameras, realistically the image is a projection of a spherical surface onto another spherical surface. This factor counteracts the effect of the radial distortion.

Using the proposed model for atmospheric geometry, one can determine the corresponding azimuth and elevation of an observed point in the sky based on its pixel location in an image. The image figure fame $\mathcal{F}$ discussed in Appendix A can be used to describe a location in the sky with pixel coordinates (x_F, y_F). The origin of $\mathcal{F}$ is defined as the top left corner of the image, F. An up-looking camera with

the top of the image plane facing north will have the 1-axis pointing West, the 2-axis pointing South, and the 3-axis pointing down.

Given a square $n \times n$ pixel image with equal longitudinal and lateral fields of view, FOV, the required simulation radius, R, can be determined using the definition of the chord of a circle. The chord length, n, forming a subtended angle, FOV, with respect to the center of a circle of radius, R, is

$$n = 2R \sin\left(\frac{FOV}{2}\right). \tag{2.22}$$

Consequently

$$R = \frac{n}{2\sin\left(\frac{FOV}{2}\right)}. \tag{2.23}$$

The distance between an observed point and the image origin in the $\mathcal{F}$ frame is

$${}^{\mathcal{F}}\mathbf{r}_{P/F} = x_F\mathbf{f}_1 + y_F\mathbf{f}_2 - R\mathbf{f}_3, \tag{2.24}$$

and the distance between the origin of the $\mathcal{F}$ and $\mathcal{B}$ frames is

$${}^{\mathcal{F}}\mathbf{r}_{G/F} = \frac{n}{2}\mathbf{f}_1 + \frac{n}{2}\mathbf{f}_2. \tag{2.25}$$

Via vector arithmetic, one will readily see that the distance between the observed point and the $\mathcal{B}$ frame origin is

$${}^{\mathcal{F}}\mathbf{r}_{P/G} = {}^{\mathcal{F}}\mathbf{r}_{P/F} - {}^{\mathcal{F}}\mathbf{r}_{G/F} = (x_F - \frac{n}{2})\mathbf{f}_1 + (y_F - \frac{n}{2})\mathbf{f}_2 - R\mathbf{f}_3. \tag{2.26}$$

One can determine the components of this vector in the $\mathcal{I}$ frame by performing the following sequence of rotations.

$$ {}^{\mathcal{I}}\mathbf{r}_{P/G} = \begin{pmatrix} x_I \\ y_I \\ z_I \end{pmatrix} = {}^{\mathcal{I}}\mathbf{R}^{\mathcal{B}}\,{}^{\mathcal{B}}\mathbf{R}^{\mathcal{F}}\,{}^{\mathcal{F}}\mathbf{r}_{P/G} \tag{2.27} $$

In (2.27), the rotation from the $\mathcal{F}$ to the $\mathcal{B}$ frame is

$$ {}^{\mathcal{B}}\mathbf{R}^{\mathcal{F}} = \begin{pmatrix} 0 & -1 & 0 \\ -1 & 0 & 0 \\ 0 & 0 & 1 \end{pmatrix}, \tag{2.28} $$

and the rotation from the $\mathcal{B}$ to the $\mathcal{I}$ frame is

$$ {}^{\mathcal{I}}\mathbf{R}^{\mathcal{B}} = \begin{pmatrix} c\psi_b c\theta_b & c\psi_b s\theta_b s\phi_b - s\psi_b c\phi_b & s\psi_b s\phi_b + c\psi_b s\theta_b c\phi_b \\ s\psi_b c\theta_b s & c\phi_b c\psi_b + s\psi_b s\theta_b s\phi_b & s\psi_b s\theta c\phi_b - c\psi_b s\phi_b \\ -s\theta_b & c\theta_b s\phi_b & c\theta_b c\phi_b \end{pmatrix} \tag{2.29} $$

where $s\psi_b = \sin(\psi_b)$, $s\theta_b = \sin(\theta_b)$, $s\phi_b = \sin(\phi_b)$, $c\psi_b = \cos(\psi_b)$, $c\theta_b = \cos(\theta_b)$, and $c\phi_b = \cos(\phi_b)$.

Based on the components of $\mathbf{r}_{P/G}$ in the inertial frame, the azimuth and elevation angles of the observed point relative to $\mathcal{B}$ can be determined. The azimuth of the observed point is

$$ \psi_p = \text{atan2}(y_I, x_I), \tag{2.30} $$

and the elevation of the observed point in the sky is

$$\theta_p = \text{acos}\left(\frac{r}{R}\right) \tag{2.31}$$

where

$$r = \sqrt{y_I^2 + x_I^2}. \tag{2.32}$$

The zenith angle of the observed point is simply

$$\zeta_p = \theta_p - 90°. \tag{2.33}$$

Once the azimuth and zenith angles of the observed point with pixel location (x_F, y_F) are known, the observation angle can be found using (2.2), provided that the solar azimuth and zenith are known. Using this observation angle, the local degree of polarization and ambient intensity are determined using (2.16) and (2.14) respectively.

The angle of polarization is determined using (2.4). A vector along the local meridian, $\mathbf{m}$, is

$$\mathbf{m} = -1\mathbf{c}_3 \tag{2.34}$$

which is along the 1-axis of the observer frame $\mathcal{B}$. To find a vector normal to the scattering plane, (2.3) is used. Letting $G \approx O$ the distance between the observed

point and O is succinctly described in the observer frame as

$$^{\mathcal{C}}\mathbf{r}_{P/O} = R\mathbf{c}_1. \tag{2.35}$$

However, $\mathbf{r}_{S/O}$ is not readily written in terms of $\mathcal{C}$. In terms of the sun frame, $\mathcal{S}$,

$$^{\mathcal{S}}\mathbf{r}_{S/O} = R\mathbf{s}_1. \tag{2.36}$$

$\mathbf{r}_{S/O}$ can be transformed to the observer frame as follows.

$$^{\mathcal{C}}\mathbf{r}_{S/O} = {}^{\mathcal{C}}\mathbf{R}^{\mathcal{I}}\,{}^{\mathcal{I}}\mathbf{R}^{\mathcal{S}}\,{}^{\mathcal{S}}\mathbf{r}_{S/O}, \tag{2.37}$$

where the rotation from $\mathcal{S}$ to $\mathcal{I}$ is

$$^{\mathcal{I}}\mathbf{R}^{\mathcal{S}} = \begin{pmatrix} \cos(\psi_s)\cos(\theta_s) & -\sin(\psi_s) & \cos(\psi_s)\sin(\theta_s) \\ \sin(\psi_s)\cos(\theta_s) & \cos(\psi_s) & \sin(\theta_s)\sin(\psi_s) \\ -\sin(\theta_s) & 0 & \cos(\theta_s) \end{pmatrix}, \tag{2.38}$$

and the transformation from $\mathcal{C}$ to $\mathcal{I}$ is

$$^{\mathcal{C}}\mathbf{R}^{\mathcal{I}} = \begin{pmatrix} \cos(\psi_p)\cos(\theta_p) & \sin(\psi_p)\cos(\theta_p) & -\sin(\theta_p) \\ -\sin(\psi_p) & \cos(\psi_p) & 0 \\ \cos(\psi_p)\sin(\theta_p) & \sin(\psi_p)\sin(\theta_p) & \cos(\theta_p) \end{pmatrix}. \tag{2.39}$$

Once the intensity, degree of polarization, and angle of polarization are computed for each pixel location, the intensities viewed through a camera with polarizing filter

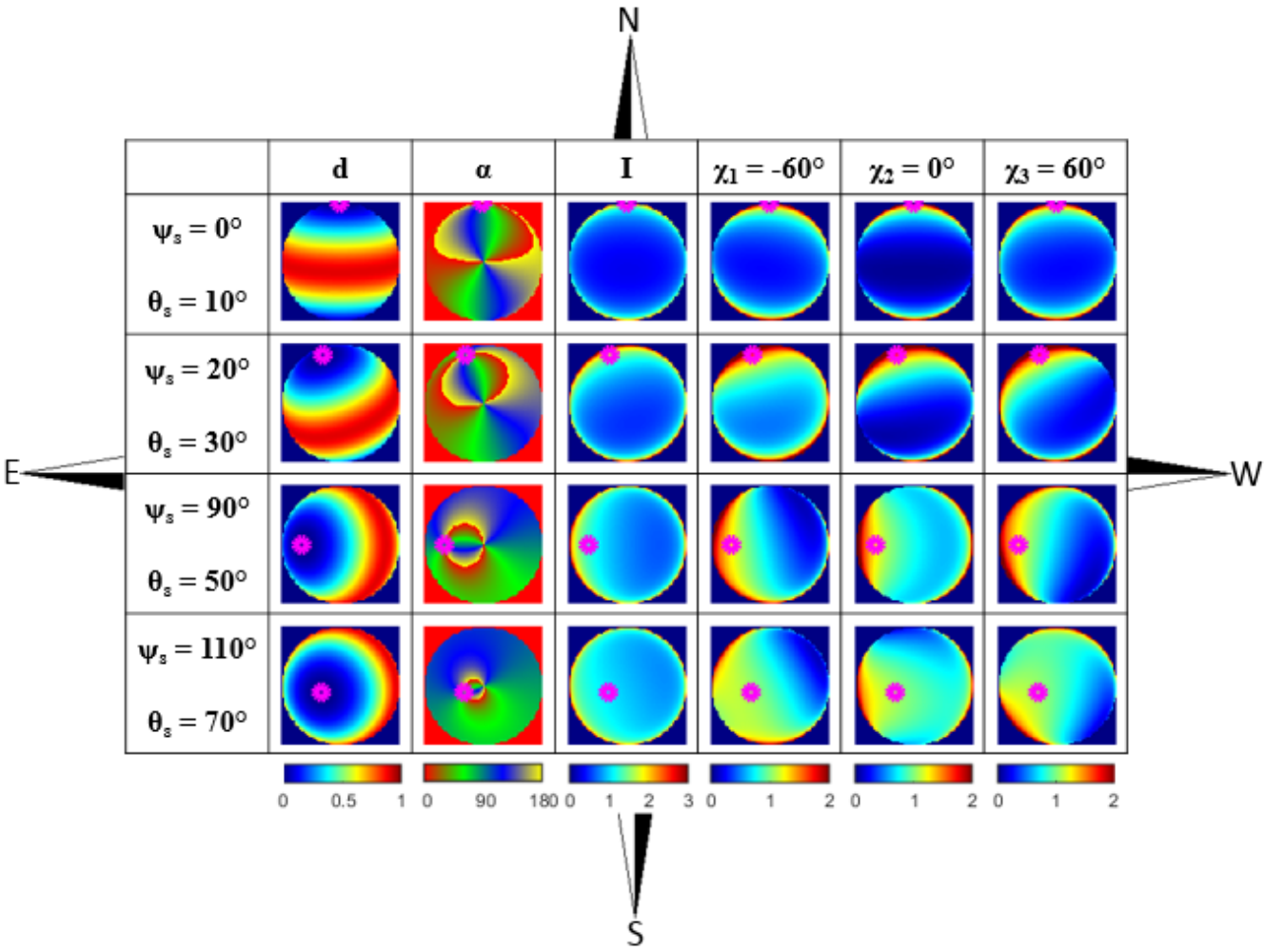

Figure 2.3: Simulated results for 4 solar positions (ψ_s, θ_s)

at orientation χ can be determined using (2.21).

Figure 2.3 shows the simulation results for 4 solar positions. For this simulation, 3 cameras with 180° field of view and 100 × 100 pixel image size are shown. The 3 cameras have filter angles at orientations of $-60°$, $0°$, and $60°$ respectively. The rigid body position of the cameras was fixed to $(\phi_b, \theta_b, \psi_b) = 0, 0, 0$.

For this simulation it was assumed that $\lambda = 0.45\mu$m, $Z_0' = 7.997x10^{-3}$m, and $d_{max} = 0.9$. The λ value was chosen under the assumption that most of the

detected atmospheric light would be in the UV to blue range. The chosen Z_0' is the calculated value for standard atmospheric conditions. d_{max} was chosen arbitrarily since it varies significantly over the course of the day. Varying d_{max} however as desired has little qualitative effect on the simulation results as shown in Table 4.3.

As shown in the simulation above, the degree of polarization exists in bands of parallels around the sun and anti-sun with the highest valued band perpendicular to the sun. The angle of polarization forms meridian line from zenith to sun and anti-sun. Angles of polarization along the solar/anti-solar azimuth are 90°, and angles of polarization perpendicular to the solar/anti-solar azimuth are $0° = 180°$.

Chapter 3: Algorithms

Atmospheric and biological principals behind how insects "see" the sky provide initial insight into how celestial cues can be used for navigation. The next piece of the puzzle is to understand how these visual inputs are converted into yaw responses. Biologists have hypothesized the existence of an internal "sky compass" [24] implying that absolute heading information can be determined based on atmospheric visual cues. Evidence supports that biological systems may use their internal circadian rhythms to predict the absolute location of the sun at any given time of day [47] [48]. Thus visual information can be used to determine heading relative to the sun, and absolute heading can be determined from the combined visual and temporal information.

There are several methods for extracting relative heading from visual atmospheric information. Insects such as Monarch butterflies have been shown to navigate using unpolarized celestial cues [20]. This might involve detection of the sun as a large bright mass in the sky and navigating relative to it. However, this could also involve making use of the predictable atmospheric luminescence patterns, or detecting chromatic gradients across the sky.

Insects such as the desert ant [16] and dessert locust [17] primarily make use of

the patterns of partially polarized light. It is likely that they are able to interpolate between the different firing rates of the ommatidia, and determine what microvilli orientation would produce the maximal firing rate. However, other neural computations are also possible. It is also feasible that insects are able to narrow in on the correct solar azimuth by saccading along the yaw axis and utilizing intensity patterns over a limited time span similar to desert ants [49]. Regardless of computational method, the angle of polarization is 180°-periodic, so there are 2 candidate heading angles for every angle of polarization. Non-polarized atmospheric cues can be used to resolve solar/anti-solar ambiguity and uniquely determine the relative solar azimuth [50]. This section discusses methods for determining relative solar azimuth and resolving solar/anti-solar ambiguity.

3.1 Polarization Based Algorithms

Polarization based algorithms make use of the patterns of polarized light throughout the sky. As can be seen from the second column of Figure 2.3, the observed angle of polarization, α, for atmospheric light increases azimuthally. Furthermore angles of polarization range between 0° and 180°, and each angle of polarization can be viewed at two unique azimuths. One will observe that the angle of polarization at both solar and anti-solar azimuths is 90°, and that an angle of polarization of 0° is found at ±90° from the solar azimuth. The 180°-periodic angle at which $\alpha = 0°$ corresponds to an imaginary line through the zenith, dividing the solar and anti-solar hemispheres. This line is termed the solar/anti-solar meridian,

and the 180°-periodic angle describing the azimuth of this line is represented as $\psi_{s/a}$.

In columns 4-6 of Figure 2.3, the cameras' vertical axes are aligned with north, and therefore the body and inertial axes are aligned. Consequently in this scenario camera filter angle, χ is also measured from north. One will notice that the overall intensity of each camera is maximal when $\chi = \psi_{s/a}$. In general, the overall intensity of a zenith facing camera will be maximized when camera filter angle is aligned with the solar/anti-solar meridian. The goal of polarization based algorithms therefore becomes to determine $\psi_{s/a}$ based on intensity measurements from a limited number of cameras each fitted with a polarizing filter at a unique orientation.

In this section, several algorithms are proposed to meet the proposed objective. The first of these methods utilizes spline interpolation, the second analytically solves for $\psi_{s/a}$ based on a model of camera outputs, and the third is a linearized version of the analytically method.

All of the methods use the average intensities of each camera as inputs. Using average intensities over a wide field of view, as opposed to individual photodiodes, allows small visual disturbances, including birds and small clouds, to be effectively filtered out. Future studies might benefit from utilizing weighted pixel averages. Weighting strategies might include the following:

1. Weighting pixel importance proportional to each pixel's corresponding elevation angle. Higher elevations would correspond to stronger weighting since Rayleigh model accuracy increases with elevation angle.

2. Pixel weighting corresponding to distance from the sun in the sky. Pixels

within a certain radius from the sun would be weighted less due to the fact that pixels in this area are generally over saturated.

3. Pixel weighting based on a quasi-HSV method. For a 3 camera system, this would work by treating each of the cameras as one of the "RGB" channels for each pixel location. Low "saturation" values correspond to low degrees of polarization which would be weighted lower. High "Value" numbers occur when at least one camera is detecting a high intensity. A pixel with a high "value" and a relatively low "saturation" is likely overexposed and should consequently be given a lower weighting. "Hue" values roughly correspond to the angle of polarization and can potentially be used as a standalone method to determine $\psi_{s/a}$.

4. The ratio of blue channel to red channel values for each pixel can be taken for each camera. Pixels with high blue to red ratios across the cameras would be weighted higher since these pixels are more likely to not correspond with cloud locations.

Many of these methods were peripherally investigated for the purposes of this thesis. They overall seemed to positively impact heading estimation accuracy. However, in an effort to increase computational efficiency they were left out of this study. These methods would likely be beneficial in a future analogue implementation of the sensor.

3.1.1 Spline Interpolation Method

The filter orientation angle at which the incoming intensity will be maximal, χ_{max}, can be found by interpolating between the intensities coming in through multiple filters, each at a different orientation angle. As the number of filters at different orientations increases, and consequently the incremental angular distance between filter angles decreases, the sinusoidal relationship between orientation angle and resulting intensity becomes approximately linear. The large spread of DRA microvilli primary orientations observed by Homberg et al. [22], and the variation of tuning directions for polarization sensitive neurons shown by Heinze et al. [30] in the supplemental material section indicate that the desert locust might in fact perform some form of linear interpolation or population coding to determine χ_{max}.

However, in the simplified model of the insect DRA proposed here, there are only 3 orientation angles, and therefore linear interpolation is no longer appropriate. Instead, spline interpolation can be used to relate the $N = 3$ average camera intensities to their respective filter orientation angle. For the vector of filter orientation angles, $\boldsymbol{\chi}$, the resulting average camera intensities, $\mathbf{y}(\boldsymbol{\chi})$, can be represented by a spline function, $s(\boldsymbol{\chi})$, which is a continuous function composed of piecewise polynomial functions, $s_i(\boldsymbol{\chi})$. Each piecewise polynomial, $s_i(\boldsymbol{\chi})$, is defined on the range, $[\chi_i, \chi_{i+1})$. Represented symbolically,

$$y(\boldsymbol{\chi}) \approx s(\boldsymbol{\chi}) = \sum_{i=1}^{N} s_i(\boldsymbol{\chi}) \mathbb{1}_{[\chi_i, \chi_{i+1})}(\boldsymbol{\chi}) \tag{3.1}$$

where the indicator function, $\mathbb{1}_A(x)$, is defined as follows for the range A.

$$\mathbb{1}_A(x) := \begin{cases} 1, & \text{if } x \in A \\ 0, & \text{if } x \notin A \end{cases} \tag{3.2}$$

There are $N = 3$ polynomial equations corresponding to the 3 filter orientation angles, χ_i, or knots, of known values. A fourth knot is required to fully define the third polynomial. Each spline, $\mathsf{s}_i(\boldsymbol{\chi})$, is chosen to be a third order polynomial, $p = 3$, of the form

$$\mathbf{s}_i(\boldsymbol{\chi}) = a_i + b_i(\chi_i - \boldsymbol{\chi}) + c_i(\chi_i - \boldsymbol{\chi})^2 + d_i(\chi_i - \boldsymbol{\chi})^3 \tag{3.3}$$

where a_i, b_i, c_i, and d_i are unknown constants to be determined. The spline function [51], $s(\boldsymbol{\chi})$, is defined such that the transition between each of the polynomials is smooth. Specifically continuity and continuous differentiability up to the $p - 1^{th}$ order are required.

$$s_i^{(n)}(\chi_i) = s_{i-1}^{(n)}(\chi_i), \quad i = 2, ..., N, \quad n = 0, 1, 2. \tag{3.4}$$

Furthermore, the interpolation conditions of the spline require that

$$s(\chi_i) = y_i, \quad i = 1, ..., N + 1. \tag{3.5}$$

The N polynomial equations, each with 4 unknown constants produce a total of $4N$ unknown constants. The constraints above will produce $4N - 2$ of these

constants. An endpoint condition is imposed to produce the remaining constants. Periodic endpoint constraints are selected since the spline function is being used to approximate a sinusoid. Periodic endpoint conditions require that

$$s^{(n)}(\chi_1) = s^{(n)}(\chi_{N+1}), \quad i = 2, \quad n = 0, 1, 2. \tag{3.6}$$

Since the sinusoid being approximating is 180°-periodic, we can let $\chi_{N+1} = \chi_1 + 180°$.

Determining the first set of constants, a_i, is very straightforward since one will notice from (3.5) that

$$y_i = s_i(\chi_i) = a_i, \quad i = 1..., N + 1. \tag{3.7}$$

The smoothness and endpoint conditions are required to determine the remaining constants. These conditions impose restrictions on the first derivative

$$\mathbf{s}_i'(\chi) = b_i + 2c_i(\chi - \chi_i) + 3d_i(\chi - \chi_i)^2,$$

and second derivative

$$\mathbf{s}_i''(\chi) = 2c_i + 6d_i(\chi - \chi_i)$$

of the polynomial functions. Now let

$$h_i = \chi_{i+1} - \chi_i, \quad i = 1..., N.$$

From the continuous differentiability of the second derivative, after some reorganiz-

ing and index substitution one will get that

$$d_i = \frac{c_{i+1} - c_i}{3h_i}, \quad i = 1..., N. \tag{3.8}$$

Next, from the continuous differentiability of the first derivative, after substituting in values from (3.8), b_i can also be solved for as a function of c_i and c_{i+1}.

$$b_i = \frac{y_{i+1} - y_i}{h_i} - \frac{(c_{i+1} + 2c_i)h_i}{3}, \quad i = 1..., N \tag{3.9}$$

Finally, from the 0^{th} order continuity condition and (3.7), (3.9), and (3.8),

$$3\frac{y_{i+1} - y_i}{h_i} - 3\frac{y_i - y_{i-1}}{h_{i-1}} = c_{i-1}h_{i-1} + 2c_i(h_i + h_{i-1}) + c_{i+1}h_i, \quad i = 2..., N-1. \tag{3.10}$$

(3.10) can also be applied to the indices $i = 1, N$ by applying the periodic endpoint condition. Since the function is assumed to be periodic, we can let $y_0 = y_N$, and $\chi_0 = \chi_N - 180°$. Consequently,

$$h_0 = \chi_1 - \chi_0 = \chi_1 - (\chi_N - 180°) = \chi_N.$$

The linear set of equation from (3.10) for $i = 1, ..N$ is used to solve for c_i. The matrix interpretation of this system of equations for $N = 3$ is

$$\begin{pmatrix} 2(h_3 + h_1) & h_1 & h_3 \\ h_1 & 2(h_1 + h_2) & h_2 \\ h_3 & h_2 & 2(h_2 + h_3) \end{pmatrix} \begin{pmatrix} c_1 \\ c_2 \\ c_3 \end{pmatrix} = \begin{pmatrix} \frac{3(y2-y1)}{h1} - \frac{3(y1-y3)}{h3} \\ \frac{3(y3-y2)}{h2} - \frac{3(y2-y1)}{h1} \\ \frac{3(y1-y3)}{h3} - \frac{3(y3-y2)}{h2} \end{pmatrix}.$$

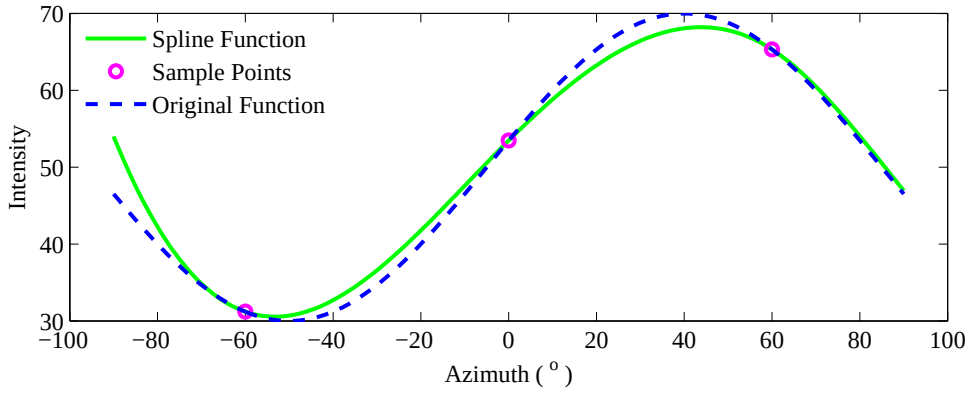

Figure 3.1: Third order spline interpolation of $y = A\cos(2(B - \chi_i)) + C$, with $B = 40°$, sampled at $\chi_1 = -60°$, $\chi_2 = 0°$, and $\chi_3 = 60°$. It is apparent that the maximum of this function is approximately $40°$ corresponding to B.

Alternately the same linear system of equations can be analytically solved for using a symbolic solver. Once the coefficients for the 3 polynomial equations are determined, $\mathbf{y}(\boldsymbol{\chi})$ can be solved for over a full 180 degree period at desired increments of χ. Figure 3.1 depicts a third order spline approximation of a sinusoidal function using the method discussed above. The member of $\boldsymbol{\chi}$ at which $\mathbf{y}(\boldsymbol{\chi})$ is maximal approximately corresponds to the filter orientation angle at which the incoming intensity will be maximal, χ_{max}, and hence the solar/anti-solar azimuth, $\psi_{s/a} = \chi_{max} + 90°$.

3.1.2 Non-Linear Analytical Method

An analytical method can alternately be used to determine the filter orientation angle at which the incoming intensity will be maximal. The relationship between average camera intensity, y_i, and the filter orientation angle χ_i through which it was measured can be modeled by the following 180°-periodic sinusoidal equation.

$$y_i = A\cos(2(B - \chi_i)) + C \tag{3.11}$$

In the above equation (3.11), A is the unknown amplitude of the sinusoid, C is the unknown vertical shift, and B is the unknown relative heading of 0° angle of polarization. The following change in variable can then be made to simplify algebraic manipulation.

$$z_i = \chi_i - \frac{\chi_3 + \chi_1}{2} \tag{3.12}$$

The consequence of this change in variable is that $z_1 = -z_3$. In this way the 3 equations modeling the 3 cameras in the form of (3.11) become

$$y_1 = A\cos(2(B + z_1)) + C \tag{3.13a}$$

$$y_2 = A\cos(2(B - z_2)) + C \tag{3.13b}$$

$$y_3 = A\cos(2(B - z_1)) + C. \tag{3.13c}$$

Using trigonometric identities, (3.13) can be rewritten as:

$$y_1 = A\cos(2B + 2z_1) + C = A\cos(2B)\cos(2z_1) - A\sin(2B)\sin(2z_1) + C \quad (3.14a)$$

$$y_2 = A\cos(2B - 2z_2) + C = A\cos(2B)\cos(2z_2) + A\sin(2B)\sin(2z_2) + C \quad (3.14b)$$

$$y_3 = A\cos(2B - 2z_1) + C = A\cos(2B)\cos(2z_1) + A\sin(2B)\sin(2z_1) + C. \quad (3.14c)$$

This system of 3 equations has 3 unknowns, namely A, B, and C. The desired unknown is B. From basic trigonometry definitions it is readily seen that

$$\tan^{-1}\left(\frac{A\sin(2B)}{A\cos(2B)}\right) = 2B,$$

and consequently

$$B = \frac{1}{2}\tan^{-1}\left(\frac{A\sin(2B)}{A\cos(2B)}\right) \quad (3.15)$$

where

$$\psi_{s/a} = B + 90^\circ.$$

The problem is now reduced to solving for the terms inside of the $\tan^{-1}$ function of (3.15). The denominator can be solved for by rearranging (3.14b).

$$A\cos(2B) = \frac{y_2 - A\sin(2B)\sin(2z_2) - C}{\cos(2z_2)} \quad (3.16)$$

The unknown variable C appearing in (3.16) can be determined by summing (3.14c)

and (3.14a) then rearranging.

$$C = \frac{y_3 + y_1 - 2y_2\cos(2z_1)}{2(1-\cos(2z_1))} \tag{3.17}$$

Finally, the numerator of the $\tan^{-1}$ function in (3.15) is then found by subtracting (3.14c) from (3.14a) and rearranging.

$$A\sin(2B) = \frac{y_3 - y_1}{2\sin(2z_1)} \tag{3.18}$$

To mitigate singularity issues, and to make use of input sign information for the $\tan^{-1}$ function in (3.15), the atan2 function was used instead. It can be shown that for 3 unique filter angles, B has precisely one singularity when using the atan2 function. The atan2 function is piecewise and defined as follows

$$\text{atan2}(a,b) := \begin{cases} \tan^{-1}(a/b), & \text{if } b > 0 \\ \tan^{-1}(a/b) + \pi, & \text{if } a \geq 0, b < 0 \\ \tan^{-1}(a/b) - \pi, & \text{if } a < 0, b < 0 \\ +\pi/2, & \text{if } a > 0, b = 0 \\ -\pi/2, & \text{if } a < 0, b = 0 \\ \text{undefined}, & \text{if } a = b = 0 \end{cases}$$

for some inputs a, and b. One will see from this definition that the atan2 function will only be undefined if both a and b are null. From (3.15), $a = A\sin(2B)$, which is defined by (3.18). This term will be null when $y_3 = y_1$, which based on the sensor

model can only be true when $\chi_1 = \chi_3$. Since it has already been assumed that all filter angles are unique, this scenario is not an option.

However, since the terms a and b are functions themselves, they must also be individually analyzed to ensure that they are always defined. a has a discontinuity when $\sin(2z_1) = 0$, or when $z_1 = \pi n, \quad n \in \mathbb{Z}$. From (3.12), one will see that this only occurs when $\chi_1 = \chi_3$, which as already stated contradicts the problem statement. b, as defined in (3.16) will have a singularity when $\cos(2z_2) = 0$, and when C is not defined. C is defined except for where $\cos(2z_1) = 1$ which is where $z_1 = \pi n$. As above, this situation will not occur. However, $\cos(2z_2)$ will take the null value when $z_2 = \pi/4 + \pi/2n$, which will occur when

$$2\chi_2 - \chi_3 - \chi_1 = \pi/2 + \pi n \tag{3.19}$$

with $n \in \mathbb{Z}$. This case *is* a theoretical possibility. For instance, if filter angles χ_1 and χ_3 were chosen to be 4° and -10° respectively, choosing $\chi_2 = 38^\circ$ would result in an undefined solution for B. In order to avoid an undefined solution in solar/anti-solar meridian B, one must make sure that the 3 chosen filter angles do not follow the relationship described in (3.19).

3.1.3 Linearized Analytical Method

A careful look at the above method will reveal that the analytical method discussed in the previous section only requires one non-linear operation. This is the inverse tangent function found in (3.15). Since the filter angles are constant,

z_i and their respective sines and cosines will also be constant. A completely linear analytical model can be achieved by finding a suitable linear approximation of the inverse tangent function. In general, an expansion of a function, $f(x)$, about a reference point x_0 is provided by the Taylor series.

$$\sum_{n=0}^{\infty} \frac{f^{(n)}(x_0)}{n!}(x - x_0)^n \tag{3.20}$$

A useful approximation of a function near reference point x_0 can be found by replacing the infinite sum upper bound with a finite integer N. The Taylor approximation of $f(x)$ generally diverges from $f(x)$ as x gets farther away from x_0. In order to more accurately approximate the inverse tangent function over a full 360° period, a piecewise function of Taylor approximations about P evenly spaced reference points can be generated. A P-piece, N^{th} order approximation of the inverse tangent function will take the form

$$\operatorname{atan}(x) \approx \sum_{p=1}^{P} \mathbb{1}_{[x_{0,p}-180°/P\ ,\ x_{0,p}+180°/P)}(x) \sum_{n=0}^{N} \frac{\operatorname{atan}^{(n)}(x_{0,p})}{n!}(x_{0,p} - x)^n$$

where $\mathbb{1}$ is the indicator function defined by (3.2). The optimal approximation, $\hat{f}(N, P, x)$, of the atan(x) function will minimize both the divergence of $\hat{f}(N, P, x)$ from atan(x) as well as the time, t_{comp}, needed to compute $\hat{f}(N, P, x)$. A simple cost function

$$J(N, P) = A||\operatorname{atan}(x) - \hat{f}(N, P, x)||_2^2 + Bt_{comp} \tag{3.21}$$

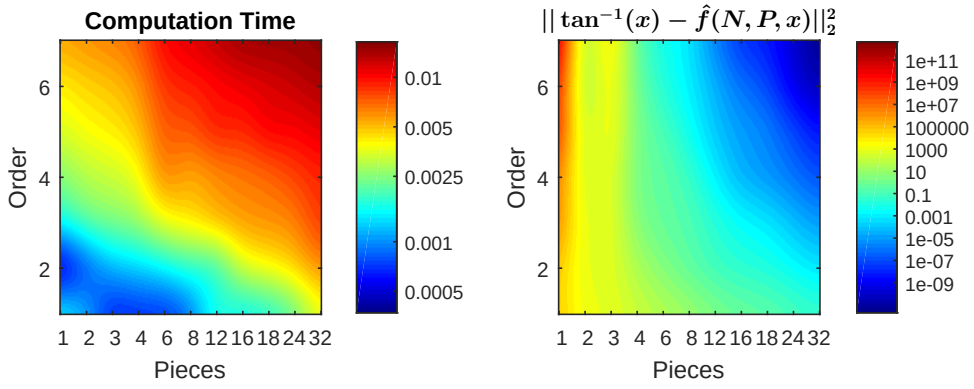

Figure 3.2: Computational time and error costs as functions of Taylor approximation order and number of piece-wise segments

with weighting constants A and B can be used for this purpose. For the constants $A = 1$ and $B = 50$, the lowest J occurred for a 16-piece second order Taylor approximation. The corresponding computational time was $t_{comp} = 0.0016$ seconds per approximation of the atan function, and the square of the normed error, $||\tan(x) - \hat{f}(N,P,x)||_2^2$, was 0.0152. Obviously different weighting constants or functions can be used in order to elicit desired performance.

Figure 3.2 depicts the computational times and norm squared errors resulting from various P-piece, N^{th} order Taylor approximations of the inverse tangent function.

3.2 Non-Polarization Based Algorithms and Hemispheric Resolution

Polarization based methods produce $\psi_{s/a}$ rather than the desired ψ_s. A non-polarization based method must be used to uniquely determine the 360° periodic ψ_s from the 180° periodic B.

One method for resolving the solar azimuth from $\psi_{s/a}$ is to make use of the chromatic gradient across the sky. There is evidence to support that the desert locust makes use of this gradient for celestial based navigation [25]. It is a known phenomenon that a higher concentration of larger wavelength light exists in the solar hemisphere, whereas the anti-solar hemisphere is dominated mostly by smaller wavelength light. For the webcam based application discussed in this paper, one can quantify this chromatic concentration by determining the ratio of red channel to blue channel intensities for all pixels. A single image is then created by summing the red:blue chromatic ratio for all 3 cameras. This image will be called $I_{r/b}$.

Additionally, the solar azimuth will also have a greater total light intensity than the anti-solar hemisphere. Making use of this fact, one can begin with the sum of grayscale images from the 3 cameras. This image will be called I_{gray}.

3.2.1 Radial Summing

The radial averaging method is based on the pattern of unpolarized celestial intensities. On a clear day, the brightest part of the sky will be where the sun is, as reflected in Figure 2.3. This is true even when the sun itself is covered by a cloud or has dropped below the horizon. Consequently, if an image of sky intensities is projected onto a plane, and if a vector $\mathbf{v}(\psi)$ is created containing all the intensities radially from zenith to horizon at a given azimuth angle ψ, then the vector along the solar azimuth $\mathbf{v}(\psi_s)$ will contain the largest average value of intensities.

In this way, a methodology for computing relative solar orientation from an

image can be achieved as follows. First, create a vector, $\boldsymbol{\psi}$, of azimuth values, ψ_i, from $-180°$ to $180°$. Assuming a square image of even side length ℓ, there will be at least one heading for every pixel along the image circumference when the length of $\boldsymbol{\psi}$ is 4ℓ. For now it is assumed that the cameras are level to the horizon, and therefore the zenith is located at the center of the image plane. Thus a set of $\ell/2$ pixels can be defined for every member, ψ_i, of $\boldsymbol{\psi}$, where the x and y coordinates in the image frame of these pixels are determined by the following:

$$\mathbf{x}(\psi_i) = \lceil \mathbf{r} \sin(\psi_i) + \ell/2 \rceil \tag{3.22a}$$

$$\mathbf{y}(\psi_i) = \lceil \mathbf{r} \cos(\psi_i) + \ell/2 \rceil \tag{3.22b}$$

In the above equation, $\mathbf{r}$ represents the length $\ell/2$ vector of distances in pixels from the zenith, and $\lceil\ \rceil$ denotes the ceiling function. This process is represented in Figure 3.3 (b).

Once a set of pixels has been assigned to every azimuth, the maximal average pixel value and its corresponding azimuth are determined to be the solar location. For a simulation with side length $\ell = 200$, the error between solar azimuth input to simulation and resolved solar azimuth output from radial summing was always within $\pm 1°$.

3.2.2 Solar/Anti-solar Hemispheric Resolution

The radial averaging method can be used as a standalone relative heading determination method. This algorithm or a simplified version of it can also be

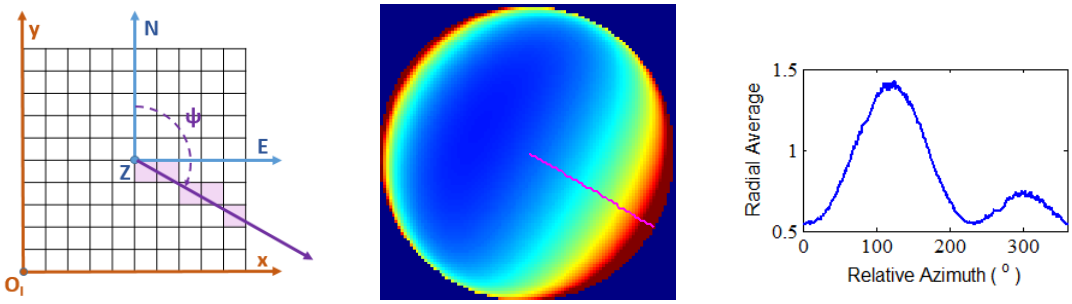

(a) (b) (c)

Figure 3.3: Resolving a summed intensity image into relative azimuth of sun. (a) Schematic of radial sum algorithm. (b) 200×200 pixel summed intensity image for $\psi_s = 120°$, $\theta_s = 25°$. Purple line indicates calculated sun orientation. (c) Results of radial sum algorithm on summed intensity image (b). Maximum averaged radial intensity estimated at relative azimuth of 120.90°. Total error of 0.90°

used in conjunction with a polarization based method to resolve solar/anti-solar ambiguity.

One such simplified version for resolving ψ_s from $\psi_{s/a}$ using either $I_{r/b}$ or I_{gray} is the image segmentation method. First the summed intensity image is divided into 9 equal square regions. A 9 pixel image is created by taking the average pixel values of these 9 regions. Next, a vector,

$$\mathbf{v} = \{v_i\}; \;\; i = 1, 2, ..., 8$$

of length 8 is created from the 9 pixel image by discarding the center pixel, and appending pixels clockwise from the top center pixel through the top left pixel. In this way the 8 components of $\mathbf{v}$ correspond to relative heading angles of $0°, 45°, ..., 315°$, and the maximum entry in $\mathbf{v}$ approximately corresponds with the solar azimuth. Otherwise stated:

$$45°(\arg\max_i\{v_i\} - 1) = \hat{\psi}_s \approx \psi_s; \;\; i = 1, 2, ..., 8.$$

Therefore if the minimum angular distance between ψ_s and $\hat{\psi}_s$ is small ($< 90°$) then $\psi_s = \psi_{s/a}$. Otherwise $\psi_s = \psi_{s/a} + 180°$.

While the above method is generally effective, decreased signal to noise ratios due to increased camera exposure settings decreases method accuracy. In such scenarios, the Radial Averaging Method discussed above can be used to find the approximate solar azimuth, $\hat{\psi}_s$, from either $I_{r/b}$ or I_{gray}.

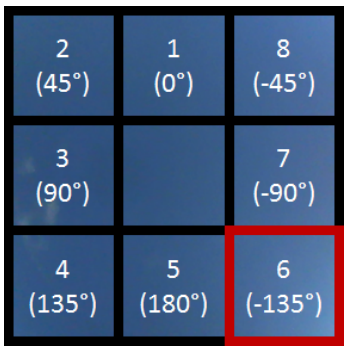

Figure 3.4: Image segmentation method

Chapter 4: Demonstration and Application of Sensing Methodology

This chapter discusses the results of applying the various heading methodologies discussed in the previous chapter for heading estimation. First the methods are applied in the simulation environment, and the results are compared for various solar elevations, image sizes, maximal degree of polarization, and polarization filter angles. Next, a hardware implementation is developed, and the various methods are applied to outdoor imagery at various conditions. The results of both simulation and outdoor experimentation demonstrate the accuracy and feasibility of using atmospheric scattering patterns for heading determination.

4.1 Simulation Results

The 3 heading algorithms were applied to the modeled camera intensity images produced by the simulation environment. For these simulations it was assumed that the solar azimuth remained fixed at 0° (north). The cameras were then rotated clockwise at 10° increments over a full 360° revolution. Radial Averaging of the summed intensity image was used for resolving the fsolar from anti-solar hemisphere.

First the effects of changes in solar elevation were analyzed. Table 4.1 shows the effect of changes in solar elevation, θ_s, on the 3 methods for 100×100 pixel

simulated images with $d_{max} = 0.9$, and $\Delta_{2/1} = \Delta_{3/2} = 60°$. It was observed that elevation changes have a negligible effect on the 2 polarization based methods, whereas performance of the radial averaging method declines with increasing θ_s.

Table 4.1: Effect of changes in solar elevation for simulation

	Radial Average			Spline Interpolation			Non-Linear		
θ_s	R^2	av|err|	σ	R^2	av|err|	σ	R^2	av|err|	σ
20	0.9965	4.08	6.32	0.9982	3.428	4.33	1.0000	0.03	0.037
40	0.9960	4.02	6.76	0.9982	3.43	4.33	1.0000	0.03	0.04
60	0.9962	3.87	6.60	0.9982	3.43	4.33	1.0000	0.03	0.04
80	0.9912	6.43	10.15	0.9982	3.43	4.33	1.0000	0.03	0.04

An assessment of the effects of image size was then performed. Table 4.2 shows the effect of changes in pixel side length, ℓ, for simulated images with $\theta_s = 20°$, $d_{max} = 0.9$, and $\Delta_{2/1} = \Delta_{3/2} = 60°$. The results indicate that the accuracy of all methods increases with increased ℓ, however the improvement is significantly more marked for the radial average method. Additionally, increasing image size slows down computational speed.

The performance of the 3 algorithms for varying degrees of polarization was then evaluated. Table 4.3 shows the effect of changes in maximum degree of polarization, d_{max}, on the 3 methods for 100×100 pixel simulated images with $\theta_s = 20°$ and $\Delta_{2/1} = \Delta_{3/2} = 60°$. It can be observed that d_{max} changes have a negligible effect

Table 4.2: Effect of changes in pixel side length for simulation

	Radial Average			Spline Interpolation			Non-Linear		
ℓ	R^2	av|err|	σ	R^2	av|err|	σ	R^2	av|err|	σ
100	0.9965	4.08	6.32	0.9982	3.43	4.33	1.0000	0.03	0.04
200	0.9988	2.93	3.68	0.9983	3.40	4.30	1.0000	0.01	0.02
300	0.9993	1.87	2.75	0.9983	3.40	4.30	1.0000	0.01	0.01
480	0.9994	1.51	2.61	0.9983	3.40	4.30	1.0000	0.00	0.01
600	0.9997	1.26	1.97	0.9983	3.40	4.30	1.0000	0.00	0.00

on the 2 polarization based methods, whereas performance of the radial averaging method slightly declines with decreasing d_{max}.

Finally the effects of changes in filter angles were considered. Table 4.4 shows the effect of changes in filter shift angles, $\Delta_{2/1}$ and $\Delta_{3/2}$, on the 3 methods for 100×100 pixel simulated images with $\theta_s = 20°$ and $d_{max} = 0.9$. As might be expected, changes in filter shift angles have little effect on the radial averaging method. Both polarization based methods appear to perform better when both Δ values are equal. Additionally the best results for the spline interpolation method appear for $\Delta_{2/1} = \Delta_{3/2} = 60°$.

Of the 3 methods, the non-linear analytical method appears to have the overall best performance for the simulation results. This is likely in part due to the fact that the model used for the simulation and for the method are nearly identical.

Table 4.3: Effect of changes in maximum degree of polarization for simulation

	Radial Average			Spline Interpolation			Non-Linear		
d_{max}	R^2	av|err|	σ	R^2	av|err|	σ	R^2	av|err|	σ
0.9	0.9965	4.08	6.32	0.9982	3.43	4.33	1.0000	0.03	0.04
0.7	0.9957	4.37	7.04	0.9982	3.43	4.33	1.0000	0.03	0.04
0.5	0.9957	4.37	7.04	0.9982	3.43	4.33	1.0000	0.03	0.04
0.3	0.9953	4.73	7.35	0.9982	3.43	4.33	1.0000	0.03	0.04
0.1	0.9950	5.14	7.59	0.9982	3.43	4.33	1.0000	0.03	0.04

In actuality this will not be the case since the variation of average intensity with heading angle is only approximately sinusoidal.

Another interesting observation is that the radial averaging method is the most sensitive to changes in elevation angle and degree of polarization. This indicates that the robustness of this method will vary significantly over the course of the day, although it will generally provide results in the correct ballpark. Based on this observation, the radial averaging method is likely not the best primary method for accurately determining solar azimuth. However, it is a reliable method for approximating solar azimuth, and thus for distinguishing the solar hemisphere from the anti-solar hemisphere.

Table 4.4: Effect of changes in filter shift angles for simulation

		Radial Average			Spline Interpolation			Non-Linear		
$\Delta_{2/1}$	$\Delta_{3/2}$	R^2	av|err|	σ	R^2	av|err|	σ	R^2	av|err|	σ
20	20	0.9965	4.08	6.32	0.9895	8.00	10.89	0.9832	12.48	14.20
40	40	0.9965	4.08	6.32	0.9958	4.92	6.79	0.9957	6.23	7.11
60	60	0.9965	4.08	6.32	0.9982	3.43	4.33	1.0000	0.03	0.04
80	80	0.9965	4.08	6.32	0.9716	12.95	17.72	0.9889	9.42	11.20
40	80	0.9965	4.08	6.32	0.9735	15.12	7.56	0.9862	9.75	7.68
80	40	0.9965	4.08	6.32	0.9819	13.39	4.58	0.9868	9.75	7.68

4.2 Stepper Motor

Outdoor experimental results were carried out to confirm simulation results as well as to determine method feasibility. The performance of the various methods were analyzed and compared under various natural outdoor conditions. During testing, maneuvering of the sensory system was accomplished using a stepper motor. Initial data sets were used to perform a one-time calibration procedure to account for human error in filter placement.

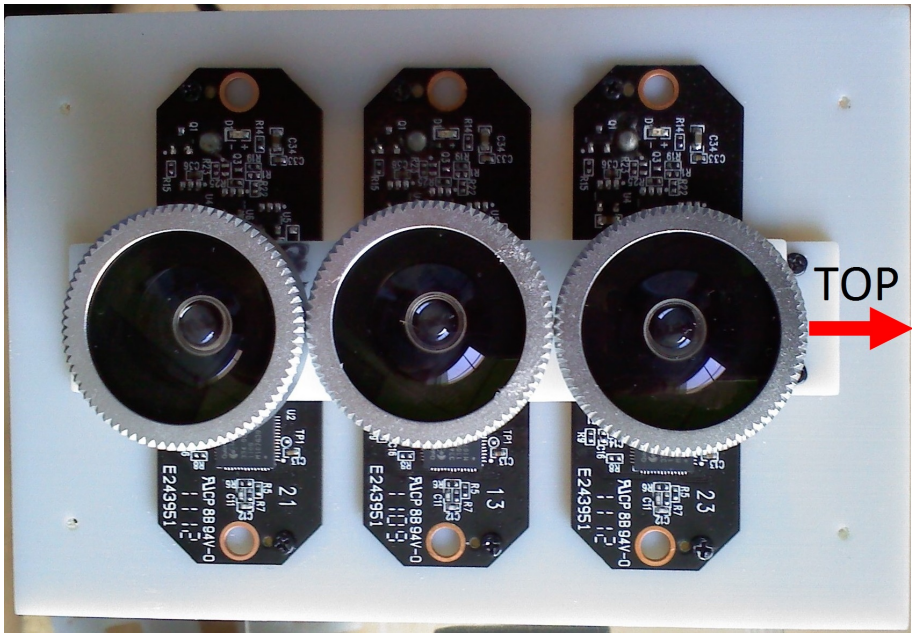

Figure 4.1: Atmospheric Sensory Unit (ASU)

4.2.1 Setup and Procedure

The experimental setup consists of an atmospheric sensory unit (ASU) modeling the insect DRA, and a stepper motor system. These are both controlled through a laptop using a Linux OS in a C++ environment.

The sensory unit (Figure 4.2) is based on three Logitech c210 USB webcams, chosen for their well supported UVC interface. The cameras are extracted from their casing and planarly mounted. A filter mount is placed above the lenses of these cameras. On the underside of the filter mount are squares of linear polarizing filter with polarization direction at angles of $-60°$, $0°$, and $60°$ from the top of the camera. Fisheye lenses are inserted above the filter mount to increase the cameras' field of view.

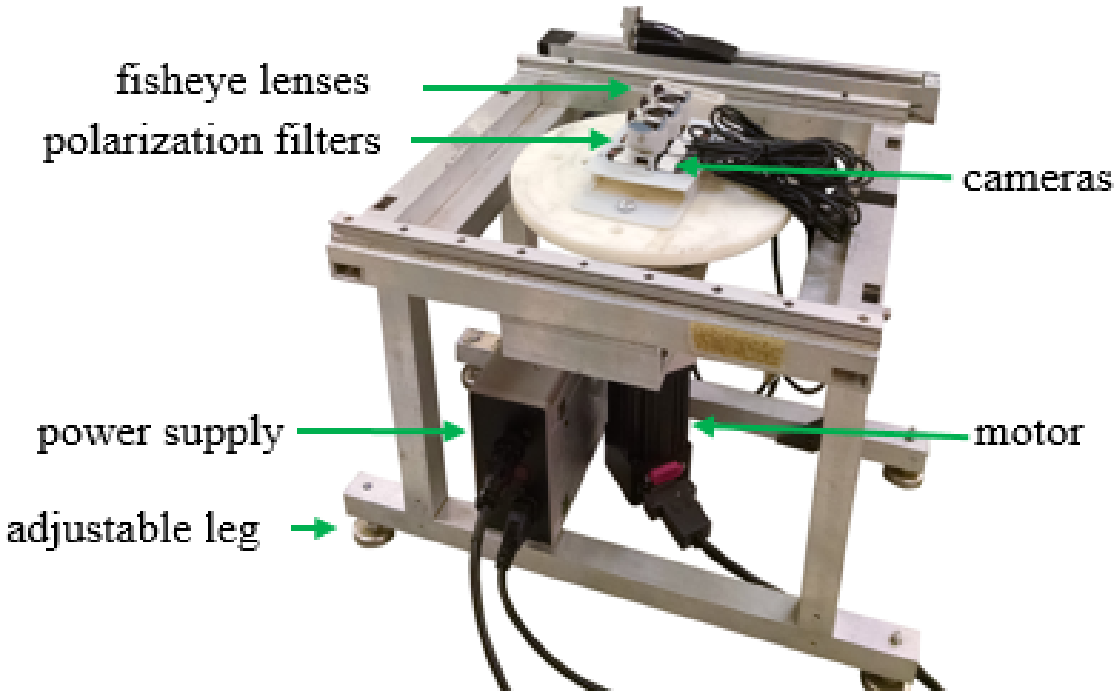

Figure 4.2: Experimental Setup

The stepper motor system is made up of an Animatics SmartMotor (SM2340D) Motor mounted to an aluminum frame with adjustable legs. The motor is fitted with a circular mounting plate, and a bull's eye level is placed on the mounting plate. The motor is powered by a 42 VDC 6 amp power supply. An RS232 cable connected to a USB adapter is used for communicate with the laptop. The ASU is affixed to the circular mounting plate.

Experiments were performed at the University of Maryland, College Park (38.990508, -76.937658) on an open courtyard. Before each experiment, the frame of the motor was aligned with a cement square of the courtyard, which served as a fixed reference frame approximately along the north/south axis. The top of the

cameras were then aligned with the motor frame so that the longitudinal axis of the image plane would be aligned with the north/south axis of the courtyard. The motor was then turned on, thereby setting the motor position origin to its current orientation. Next, the pegs of the motor frame were adjusted to align the image plane of the ASU with the horizon.

At the beginning of each experiment the current local time was acquired, and the current solar position was computed using the freely available C++ files provided by PSA [52]. The stepper motor would then complete a full 360° rotation in either 5° or 10∘ increments every 3 seconds, providing ample time for motor oscillations to fully damp out and all serial signals to be sent and received. Preceding each motor increment, the following steps occurred: 1) frames from each camera were captured, 2) relative solar azimuth was computed using the three methods discussed above, and 3) current motor encoder position was retrieved and converted to degrees. All acquired data was logged and saved to the laptop.

4.2.2 Calibration Results

Before data was analyzed, a calibration was performed to verify whether or not the polarization filters were oriented as expected, and how close with true north the cameras were initially aligned. Calibration only needs to occur once in the lifetime of the sensor system assuming parts are not replaced. The following describes to calibration procedure.

First, for each camera, i, of each test, the set of average image values, $\mathbf{y}_i$, and

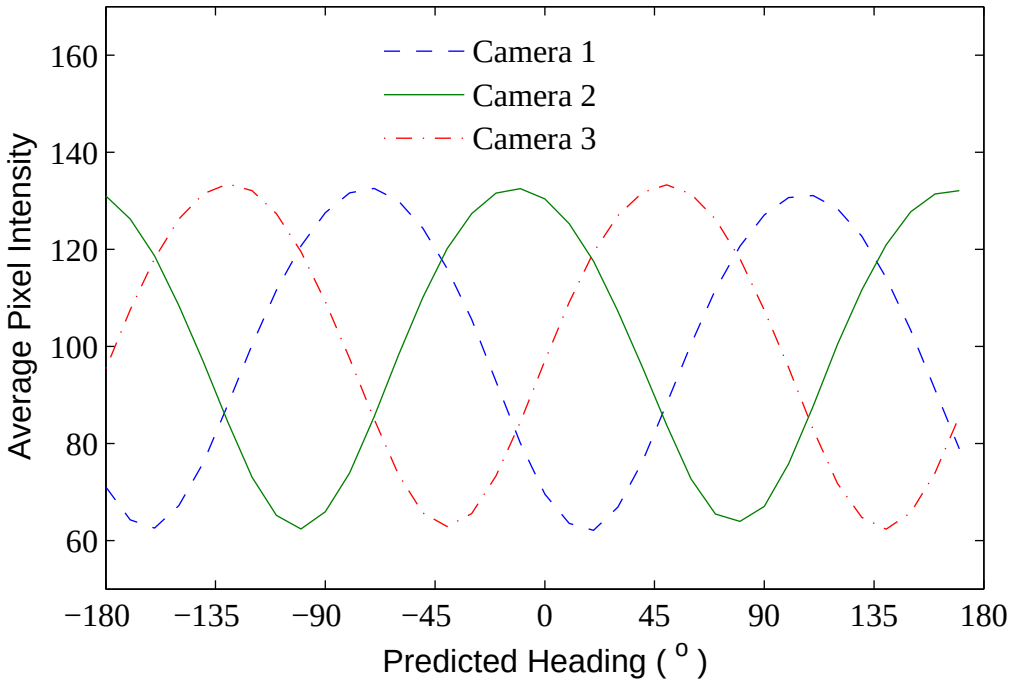

Figure 4.3: Pixel averages over full 360 degree turn for each camera

corresponding motor position, $\boldsymbol{\psi}_m$, were fit to a sinusoidal function of the form

$$\mathbf{y}_i = A_i \cos(2(\boldsymbol{\psi}_m - B_i)) + C_i; \;\; i = 1, 2, 3. \tag{4.1}$$

Figure 4.3 depicts the relationship between average image intensity and motor position over a full 360° rotation.

Function fitting was accomplished using the MATLAB® 'fmincon' function by varying A, C, and ψ_m, where A was constrained to be positive and B_i was constrained to be within a 360° range. Since the desired orientation of camera 2 is 0°, $B_2 - \psi_s$ should be zero if the filter is placed as desired, and the longitudinal camera axis is properly aligned with the north/south axis. Alternatively, the sum

of these 2 errors is

$$\Delta_2 = B_2 - \psi_s. \tag{4.2}$$

An average Δ_2 value of $-8.32°$ with standard deviation of $2.56°$ lends to the conclusion that the initial reference position is about $10°$ west of true north.

Next the relative positions between filter orientations were determined where $\Delta_{2/1}$ and $\Delta_{3/2}$ are the angular distances between filters 1 and 2, and filters 2 and 3 respectively. The average $\Delta_{2/1}$ value was found to be $65.68°$ with a standard deviation of $2.76°$, and average $\Delta_{3/2}$ value was found to be $62.36°$ with a standard deviation of $4.83°$. This implies that relative filter positions where within $\pm 8°$ of expected. The magnitude of the standard deviations is likely due to image noise and confusion from artificial light sources for tests taken around and after sunset.

As a result of this calibration, χ_1, χ_2, and χ_3 were taken to be $24.32°$, $90°$, and $152.26°$ respectively. These values were plugged into the algorithms for the captured frames and used to calculate heading values.

Generally when dealing with multi-camera systems, geometric and intensity calibrations are performed in order to provide consistency between the pixels of all of the cameras and thus increase measurement accuracy. Geometric calibration provides information about each camera's focal length, principal point, and image distortions. Geometric calibration allows image flattening, determination of variation in pixel size, as well as a comparison of position and scaling between cameras. Intensity calibration accounts for the fact that different pixels will return different

pixel values when presented with the same intensity of light. Furthermore, accumulation of dust and lens deformities might also cause varying pixel responses.

While the increased accuracy provided by geometric and intensity calibrations is desirable, it was determined that obtaining a useful calibration was not practical. Both calibration require near identical camera configuration during calibration and experimentation. Since no straightforward method to disable autofocus without rewriting the camera driver existed, it was impossible to guarantee consistent camera configuration. Furthermore, the results of geometric calibration, especially distortion constants, are only valid for a range of object at distances comparable to those used for calibration. Since the objects of interest are air particles at various locations throughout the atmosphere, developing a geometric calibration rig proved challenging. However, as object distances from camera increase, the significance of planar distance between cameras decreases. Finally, intensity calibration generally requires a "flat field" image which is taken at about the same exposure as the experimental images are taken without underexposing or saturating the pixels. A rig for creating nearly flat field images was constructed. However use of the calibration results had a negligible effect on heading estimation, and thus the obtained intensity calibration constants were not used.

4.2.3 Results

A total of 77 tests were performed following the procedure outlined in section 4.2.1 above. These tests were performed for solar elevations ranging from $-5°$

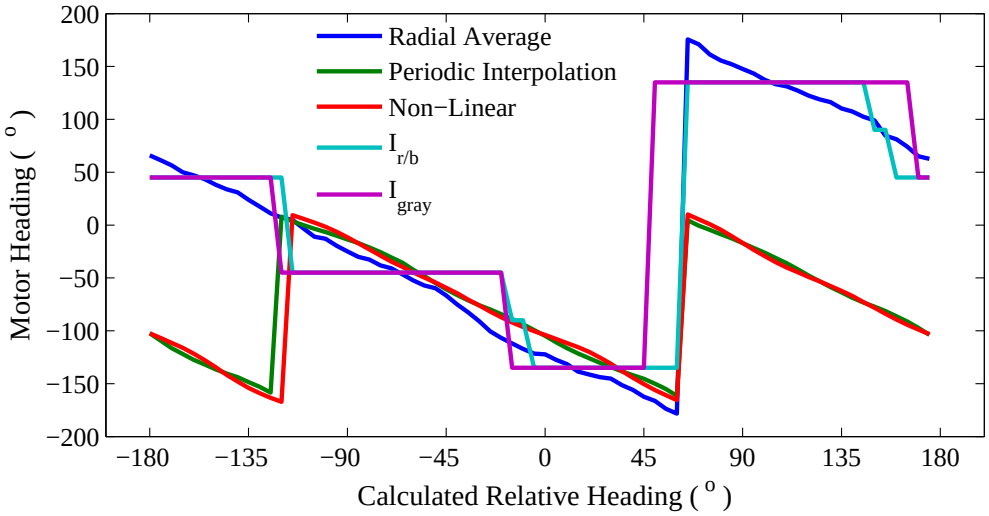

Figure 4.4: Overview of azimuth finding and hemispheric resolution methods

to 53°, camera exposures ranging from 1 to 500, and varying levels of cloudiness. Captured frames of size 640 × 480 were cropped to square 480 × 480 images, and heading calculations were performed during testing to assess feasibility of real time processing. However, the results of these calculations were not used for analysis purposes as calibration values had not yet been computed.

For each test, relative heading calculations for each of the methods were performed at every motor position increment. Figure 4.4 shows results for the 3 solar azimuth finding methods and the 2 hemispheric resolving methods for a single test. The test was taken for a solar elevation of 16.6° and an exposure value of 10. One can observe that the hemispheric resolving methods correctly follow the trend of the Radial Averaging method.

Hemispheric resolution methods were then applied to the polarization based

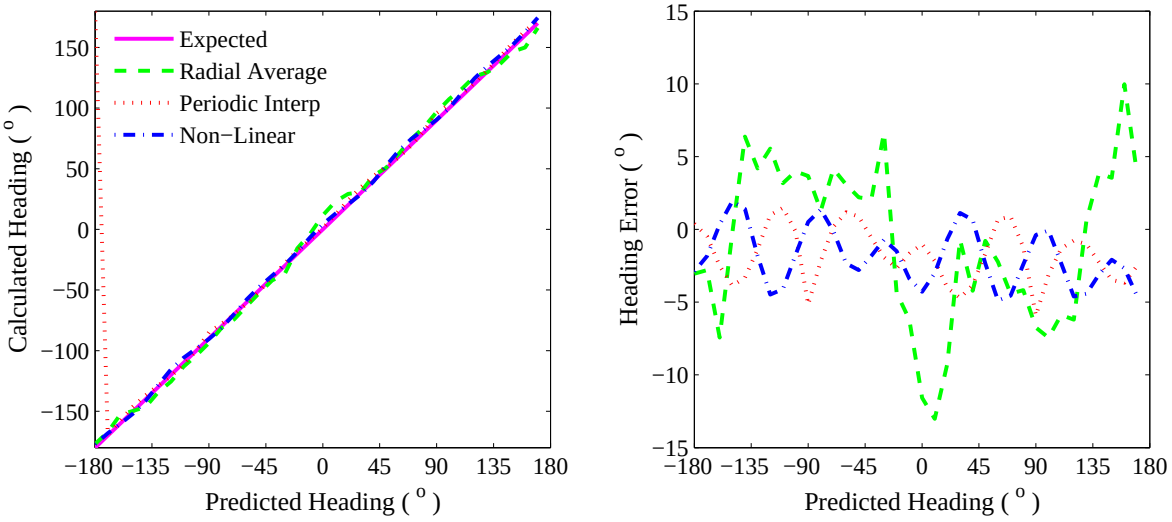

Figure 4.5: Comparison of methods over 360 degree turn at 10 degree increments

azimuth finding results. Absolute heading measurements for all methods were computed by applying the computed solar azimuth [53]. The calculated absolute heading values were compared with the expected absolute heading values in order to quantify the individual measurement errors as well as the overall method performance. Figure 4.5 shows the results for another test. The average of the absolute value of errors was determined for each test as a measure for comparing method performance between tests.

It was observed that the heading methods all appeared to work with relative reliability even for negative solar elevations and in the presence of clouds. However, when the vast majority of the sky was covered with clouds, none of the methods produced useful results as might be expected. Stratus clouds had minimal impact on results, while cumulus clouds noticeably increased sensor error. Sensitivity to

clouds was markedly most noticeable for the radial averaging method, and affected the polarization based methods almost equally.

The increased cloud sensitivity of the radial averaging method is likely due to the fact that the RGB values for the color white correspond to a high grayscale luminance value. Additionally, clouds reflect more light than the rest of the sky does. The combination of these two factors can have the effect of making the algorithm choose a cloud as the brightest region in the sky thereby confusing the solar azimuth with a nearby cloud's azimuth. It has been shown that atmospheric scattering patterns penetrate clouds better for smaller wavelength light [36]. It is likely that insects primarily rely on UV wavelengths for this reason. The methods presented here rely on the full visible spectrum detected by the cameras since it was noticed that the cameras' blue channels were very noisy and unreliable.

Next the relationship between measurement error and solar elevation was analyzed for several different exposure settings. Since as solar elevation increases, degree of polarization decreases, it was expected that solar elevation would be proportional to measurement error. As can be seen in Figure 4.6, a nearly exponential relationship was observed for the polarization based methods. From the data presented, solar elevation does not appear to clearly affect the radial averaging method.

A similar analysis was performed in order to analyze the effect of image exposure as shown in Figure 4.7. For the polarization based methods, measurement error appears to sharply decrease with increasing exposure then level off, while a slightly positive relationship between measurement error and exposure appears to be present for the radial averaging method. However, it can be observed that the

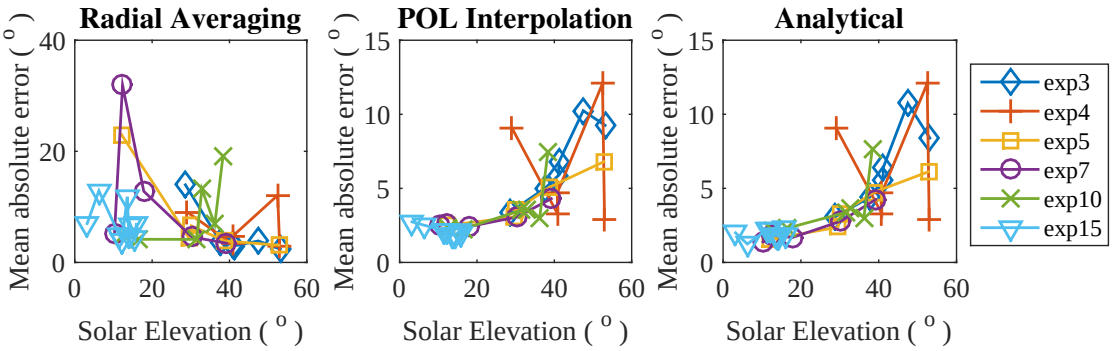

Figure 4.6: Effects of solar elevation on method error

sharp downwards ramp is comprised of high solar elevation data where the ambient light is primarily not polarized.

When the image sensor is underexposed, it is logical that that the image sensor primarily responds to the unpolarized light and does not detect all of the polarization information. Furthermore one will recall that the radial averaging method presented relies on polarized images. Since this method is based on unpolarized light, it is understandable that increasing exposure, and thereby decreasing the ratio of unpolarized to polarized light information, will decrease the reliability of the method. A single unfiltered camera could be used in order to increase sensor accuracy when primarily relying on the radial averaging method for determining heading. Nonetheless, it can be observed from this data that for a single solar elevation, a fairly large range of exposure values will produce similar results.

Finally the overall performance of the different methods was compared by taking the average of error, standard deviation, and R^2 values for all tests for each method. Table 4.5 shows a method comparison for 50 of the total 77 tests. Tests

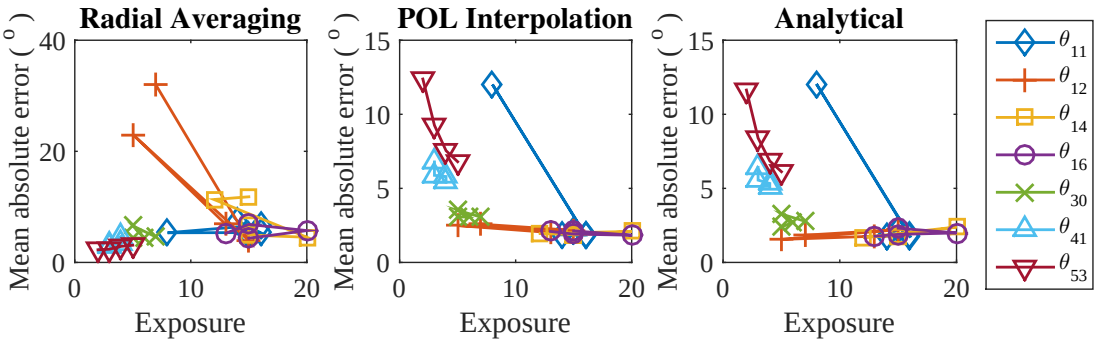

Figure 4.7: Effects of exposure on method error

in which images contained relatively large cumulus clouds or significant image saturation were excluded from this analysis. These results indicate an overall more reliable performance for polarization based methods as compared to the radial averaging method.

Table 4.5: Summary of Results

	Radial Average	Spline Interpolation	Non-Linear
Average |Error| (°)	6.61	3.26	3.00
Min Error(°)	2.98	1.75	1.24
Max Error(°)	36.92	12.01	12.05
Standard Deviation (°)	6.81	4.05	3.70
R^2	0.9913	0.9977	0.9979
n	50	50	50

The results presented above show that the developed algorithms are feasi-

ble and practical methods for determining absolute heading based on atmospheric scattering. Improvements can be made by performing camera calibration to obtain intrinsic and extrinsic parameters for all cameras, in addition to calibrating individual pixel responses. To obtain useful calibration results, the camera lens configurations must be the same during calibration as for data acquisition. Since there is no straightforward way to disable autofocus on the webcams used here, camera calibration has not been performed. Overall performance can likely be improved by using better quality cameras or by including a model of measurement noise in the calculations.

Chapter 5: Control

This chapter discusses implementations of heading algorithms on various platforms, real and simulated, for closed loop heading control. Platforms include a differential drive ground robot and simulated MAV quadrotor.

5.1 Ground robot

The ASU was implemented on a differential wheeled terrestrial robot to demonstrate real time autonomous heading control of a vehicle. Robot heading was measured and controlled using the atmospheric scattering based methods discussed in Chapter 3. Verification of these methods is provided through alternate heading measurement techniques, including use of a magnetometer and wheel encoder information. This section begins by detailing the experimental setup. The methods for acquiring alternate heading measurements are then provided. Finally the test procedure is described, and the results are analyzed.

5.1.1 Setup

A modified Dr. Robot X80 mechanical construction set was used as the test platform. The X80 was equipped with two 12V geared DC motors along with DC

motor driver modules with position and current feedback, servos, and 1200 count per wheel cycle optical encoders. Interfacing with the motors was achieved via a PMS5005 robot sensing and motion controller. The X80 system was powered by a 7.2V Ni-MH 3800mAh battery pack. An RS232 interface module and RS232 cross-over serial cable were used to directly communicate with the PMS5005 and the on board PC.

The on board PC was composed of an ASUS M5A78L-M LX PLUS mother-board equipped with a 4GB single DDR3 240-pin memory module and AMD Athlon II X2 270 Regor 3.4 GHz Dual-Core Desktop Processor. The PC was powered by a 4 cell 15V 5A lithium-ion battery. An internal USB to external USB female port cable was installed to provide access to additional USB hubs and therefore better distribute CPU for devices.

The ASU was mounted planarly atop the robot with the vertical axes of the cameras parallel to the body 1-axis of the robot. The robot was also equipped with a Pololu MiniIMU-9 v2 gyro, accelerometer, and compass. The Minimu was mounted on an 8 cm post to mitigate electromagnetic interference from the robot in magnetometer readings. A Deventech USB to I2C adapter and an USB A to USB B cable were used for interfacing and communication between the PC and the magnetometer.

The robot was also equipped with an USB wifi dongle. This allowed the creation of an adhoc network between the robot's PC and a laptop. Through this network, robot heading control test sequences could be initiated via PuTTY SSH and TightVNC Viewer.

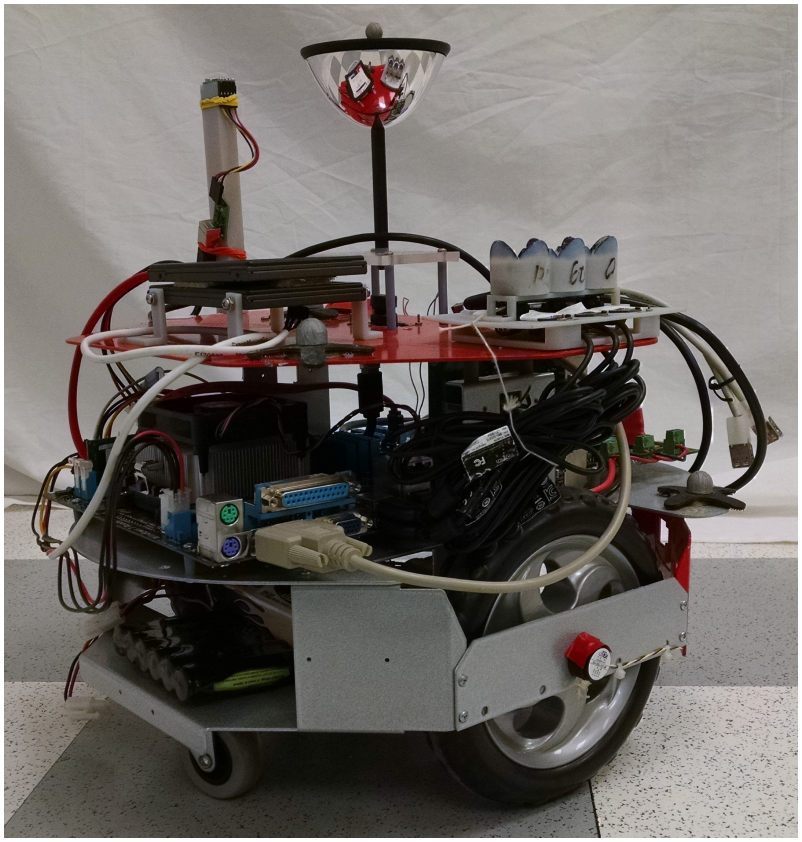

Figure 5.1: Ground Robot Configuration

5.1.2 Magnetometer Calibration

A 3-axis magnetometer, such as the one on the Pololu Minimu-9 board, measures the strength of the surrounding magnetic field along three perpendicular directions. Whilst navigating on earth's surface, heading can be determined relative to earth's magnetic poles by measuring earth's magnetic field. A magnetometer will measure earth's magnetic field, but it will also measure all other local electromagnetic fields. It is not practical to exclusively measure the effects of earth's magnetic field while in motion. However the near constant fields effects due to material imperfections of the magnetometer, and the additional electronic hardware on the robot can readily be corrected for. Shifts or biases in the field are called hard iron distortions, while stretches and deflections are called soft iron distortions. The purpose of magnetometer calibration is to remove the effects of these hard and soft iron distortions.

If one were to plot the measurements of an ideal magnetometer at all possible orientations in 3D Cartesian space, one would get a sphere centered at (0,0,0). The measurements of a magnetometer subject to hard and soft iron distortions approximately maps to an ellipsoid not necessarily centered at the origin. The equation for such an ellipsoid is described by (5.1).

$$ax_m^2 + by_m^2 + cz_m^2 + 2dx_m y_m + 2ex_m z_m + 2fy_m z_m + 2gx_m + 2hy_m + 2iz_m = 1 \quad (5.1)$$

In (5.1), x_m, y_m, and z_m are measurements from the 3 axes of the magnetometer,

and a through i are unknown coefficients to be solved for. These coefficients can be solved for using the solution to the linear least squares problem (5.2)

$$\hat{\mathbf{\Theta}} = (\mathbf{X}^T\mathbf{X})^{-1}\mathbf{X}^T\mathbf{v} \tag{5.2}$$

where $\hat{\mathbf{\Theta}}$ is an estimate of the parameter vector

$$\mathbf{\Theta} = [a \;\; b \;\; c \;\; d \;\; e \;\; f \;\; g \;\; h \;\; i]^T,$$

the regressions, $\mathbf{X}$ are

$$\mathbf{X} = [x^2 \;\; y^2 \;\; z^2 \;\; 2xy \;\; 2xz \;\; 2yz \;\; 2x \;\; 2y \;\; 2z]^T,$$

and the output, $\mathbf{v}$, or right hand side of (5.1) is an array of ones

$$\mathbf{v} = \mathbf{1}.$$

In matrix notation, the ellipsoid equation can be written in the following form as in [54] and Yuri Petrov's "ellipsoid fit" function available on MATLAB® Central.

$$\mathbf{x}^T A\mathbf{x} + 2B^T\mathbf{x} + c = 0 \tag{5.3}$$

where

$$A = \begin{bmatrix} a & d & e \\ d & b & f \\ e & f & c \end{bmatrix}, \quad B = \begin{bmatrix} g \\ h \\ i \end{bmatrix}, \quad C = 1, \quad \mathbf{x} = \begin{bmatrix} x_m \\ y_m \\ z_m \end{bmatrix}.$$

The ellipsoid can be rotated and translated by introducing a new set of coordinates $\tilde{\mathbf{x}}$ such that

$$\mathbf{x} = R\tilde{\mathbf{x}} + \mathbf{t}. \tag{5.4}$$

Letting $\tilde{A} = R^T AR$, $\tilde{B} = (2\mathbf{t}^T A + 2B^T)R$, $\tilde{C} = \mathbf{t}^T A\mathbf{t} + 2B^T\mathbf{t}$, and after rearranging, (5.3) may be written as

$$\tilde{\mathbf{x}}^T \tilde{A}\tilde{\mathbf{x}} + \tilde{B}^T\tilde{\mathbf{x}} + \tilde{c} = 0 \tag{5.5}$$

Choosing $\mathbf{t}$ such that $\tilde{B} = 0$, the ellipsoid centroid is simply $\mathbf{z} = \mathbf{t} = A^{-1}B$. Then applying the principal axis theorem to the first term in (5.5), it is known that the eigenvectors of $\tilde{A}$ correspond to the directions of the principal axes of the ellipse. It then follows that the lengths of the axis correspond to the eigenvalues as

$$r_1 = \sqrt{-\tilde{c}/\lambda_1}, \quad r_2 = \sqrt{-\tilde{c}/\lambda_2}, \quad r_3 = \sqrt{-\tilde{c}/\lambda_3}$$

where λ_i are the eigenvalues of $\tilde{A}$. The corrected magnetometer values, $\mathbf{x}_{cal}$, are

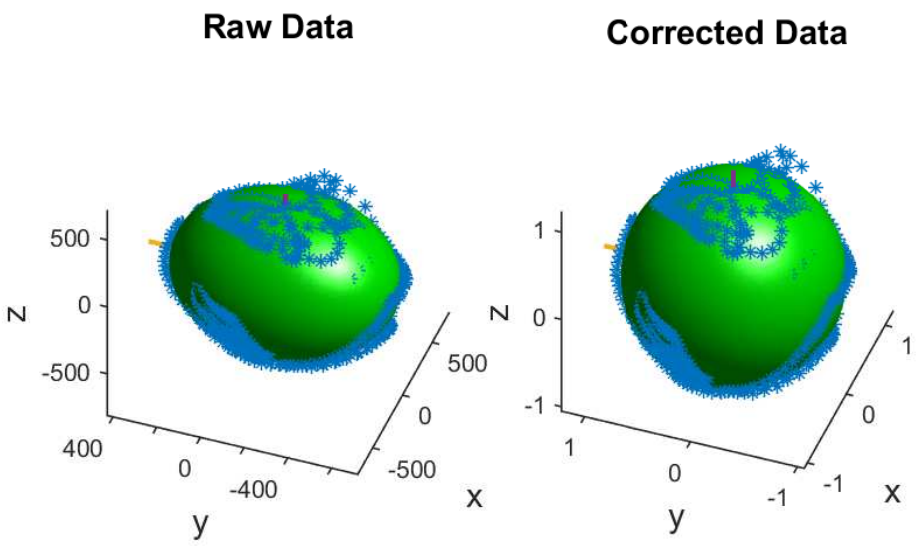

Figure 5.2: Raw and corrected magnetometer calibration data fit to ellipsoids

then computed as

$$\mathbf{x}_{cal} = \tilde{A}^{-1}\mathbf{x} - \mathbf{z}.$$

Figure 5.2 shows the raw calibration data and the ellipsoid it's fitted to, as well as the resultant spherical data once the data has been corrected. For a magnetometer with x, y, and z axes aligned with the vehicle North-East-Down body axes, the magnetic heading is simply

$$\psi_m = \tan^{-1}(y_m/x_m).$$

5.1.3 Wheel Encoder Calibration

A wheel encoder produces an output proportional to the angular position of the wheel relative to the wheel's starting position. On a homogeneous surface, wheel encoder values will be directly related to the distance traveled by the wheel. Furthermore, if continuous readings of encoder values are available, a comparison between incremental encoder values of the wheels of a differential wheeled robot can be used to determine the angular distance that the robot has traveled over time. Otherwise stated, differential changes in robot linear angular distances are proportional to differential changes in wheel encoder values. Symbolically,

$$\dot{\boldsymbol{\psi}} = K_1 \mathbf{v}_L + K_2 \mathbf{v}_R \tag{5.6a}$$

$$\mathbf{u} = K_3 \mathbf{v}_L + K_4 \mathbf{v}_R \tag{5.6b}$$

where $\mathbf{v}_L$ and $\mathbf{v}_R$ are left and right wheel encoder rates respectively, $\dot{\boldsymbol{\psi}}$ is angular distance rate or yaw rate, $\mathbf{u}$ is forward speed, and K_1, K_2, K_3, K_4 are unknown constants. The values of these constants can be determined using linear least square regression. (5.2) provides the solution to the linear least square problem where,

$$\mathbf{X} = [\mathbf{v}_L \ \mathbf{v}_R]$$

for $\mathbf{z} = \dot{\boldsymbol{\psi}}$, $\hat{\boldsymbol{\Theta}} = [K_1 \ K_2]^T$, and for $\mathbf{z} = \mathbf{u}$, $\hat{\boldsymbol{\Theta}} = [K_3 \ K_4]^T$. (5.6) can then be used to determine the total angular,ψ_{enc}, and inertial distances, x_{enc} and y_{enc}, traveled at

any time, t_i, where

$$\psi_{enc}[t_i] = (K_1 v_L[t_i] + K_2 v_R[t_i])(t_i - t_{i-1}) + \psi_{enc}[t_{i-1}] \tag{5.7a}$$

$$x_{enc}[t_i] = (K_3 v_L[t_i] + K_4 v_L[t_i]) \cos(\psi_{enc}[t_i]) + x_{enc}[t_{i-1}] \tag{5.7b}$$

$$y_{enc}[t_i] = (K_3 v_L[t_i] + K_4 v_L[t_i]) \sin(\psi_{enc}[t_i]) + y_{enc}[t_{i-1}] \tag{5.7c}$$

for $i > 0$, and $\psi_{enc}[t_0] = x_{enc}[t_0] = y_{enc}[t_0] = t_0 = 0$. These distances can be used for robot trajectory control, and ψ_{enc} can be used to verify atmospheric scattering based heading estimations.

For the purposes of this system identification, vehicle states were tracked using a Vicon motion capture system consisting of 8 T-series cameras. The Vicon system determines the positions of reflective markers attached to the robot via triangulation at a rate of 350 Hz. Relative positions of the markers are used to find the rigid body states of vehicle including $\dot{\boldsymbol{\psi}}$ and $\mathbf{u}$. $\mathbf{v}_L$ and $\mathbf{v}_R$ were retrieved from the PMS5005 and recorded along with a time stamp. While data was collected, the robot was remotely given commands to turn left and right, and to increase and decrease forward speed.

After data collection, the average time difference between encoder velocity measurements was determined and used in order to down sample the Vicon state measurements. Data cropping was also performed in order to make sure that measurements from Vicon and PMS5005 of initial robot motion were aligned, and that $\mathbf{z}$ and $\mathbf{X}$ were the same length.

SIDPAC [55] was then used to perform linear least square regression and statistical analysis, including consideration of colored residuals. The parameters resulting

from this analysis are shown in Table 5.1.

Table 5.1: Wheel encoder coefficients

Parameter	Estimate	Std Error	% Error
K_1	1.596×10^{-3}	5.765×10^{-5}	3.6
K_2	-1.617×10^{-3}	4.441×10^{-5}	2.7
K_3	2.202×10^{-4}	7.339×10^{-6}	3.3
K_4	2.183×10^{-4}	5.716×10^{-6}	2.6

Figure 5.3 shows a comparison between the true yaw rate and forward velocity and the estimates calculated using (5.6).

Figure 5.4 depicts the traveled angular distance, ψ_{enc} of the robot as well as the inertial trajectory of the robot. Estimates were determined following (5.7).

The figures shown above indicate good correlation between the estimates and true values. Low percent errors, and standard errors of two orders less than the parameter estimates, further indicate satisfactory model determination.

5.1.4 Procedure

Ground robot tests were performed in the courtyard of the Kim Engineering Building at University of Maryland, College Park. Before each test, an ad-hoc network was created between the robot and a laptop. PuTTY and TightVNC were then used to establish secure remote communication. Next the wheels of the robot

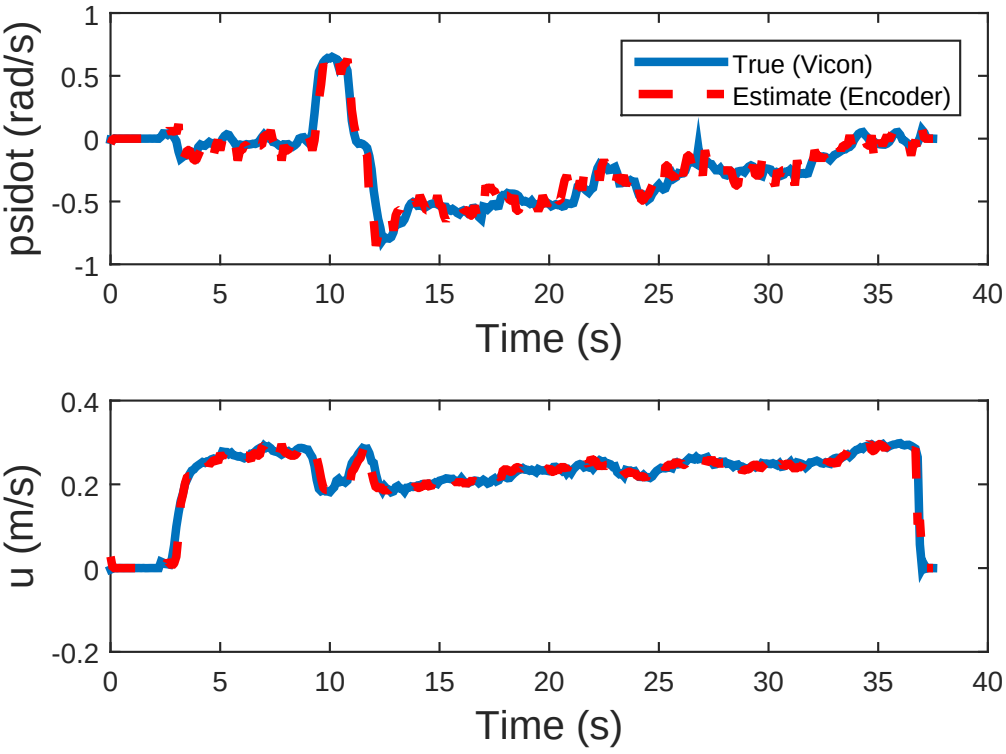

Figure 5.3: True and estimated yaw rate and forward velocity

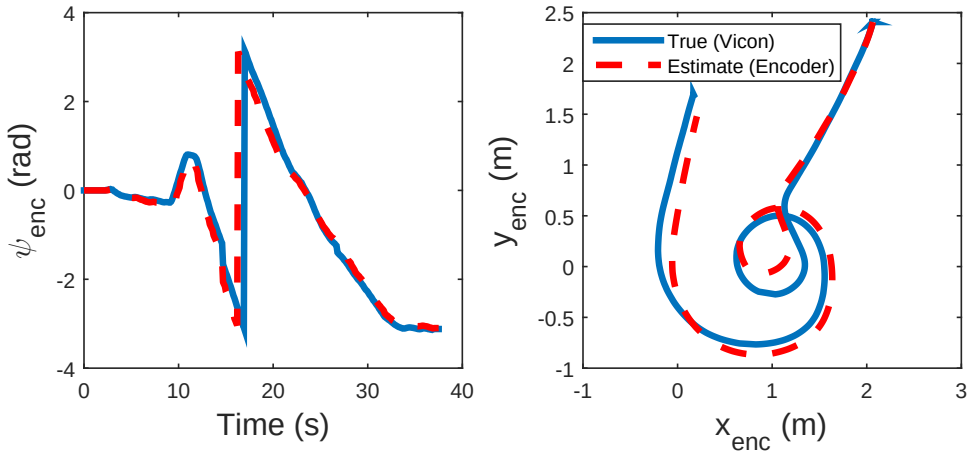

Figure 5.4: True and estimated total yaw and position

were aligned with the edge of a cement square of the courtyard. In addition to the fact that the edges of these squares are approximately coincident with the cardinal compass directions, the squares also served as a visual reference that the robot was maintaining heading. Commands were then sent through the laptop to establish which heading estimate methodology would be used for control, and to initialize the robot test procedure.

The robot test procedure began by starting and setting the cameras of the ASU. Communication was then initialized and established with the wheels of the robot. Next, initial heading estimates were determined and recorded using the various methodologies discussed in Chapter 3. Additionally a heading measurement from the magnetometer, and a relative heading approximation from the wheel encoders were also acquired and recorded. A timer was then initialized, and the robot was then commanded to proceed forward at a constant speed, v_F, and maintain heading. Until a termination command was received, the following sequence of steps were iterated.

1. Images from the ASU cameras were acquired.

2. Current solar position computed using ephemeris function

3. Atmospheric scattering based algorithms were used to calculate heading estimates, and results were recorded.

4. Magnetometer measurements were taken, and magnetic heading was computed

5. Wheel encoder positions were read, recorded, and used to approximate relative

heading from initial heading

6. Total time since timer initialization was determined and recorded.

7. Wheel speed commands, based on current heading error, were generated and sent.

Inputs to the Dr. Robot were serial words encoding desired right and left wheel speeds as encoder rates. Ideally equal encoder rates sent to both wheels would result in straight motion, while a greater right wheel speed would result in a left turn and a greater left wheel speed would result in a right turn.

Wheel speed commands were computed as offsets from the desired forward constant speed distributed evenly between both wheels, v_F.

$$\begin{aligned} v_{L,cmd} &= v_F - \dot{\psi}_{cmd} \\ v_{R,cmd} &= v_F + \dot{\psi}_{cmd} \end{aligned} \tag{5.8}$$

A heading hold algorithm using a discrete PID controller of the following form was used to generate the yaw offset, ψ_d at each time step, t_i

$$\dot{\psi}_{cmd}[t_i] = K_p e[t_i] + K_i \sum_{j=1}^{i} e[t_j] + K_d \frac{e[t_i] - e[t_{i-1}]}{t_i - t_{i-1}} \tag{5.9}$$

where $e[t_i] = \psi_d[t_i] - \psi_e[t_i]$ and $e[t_0] = t_0 = 0$. The desired heading, ψ_d, was initialized to the first heading measurement, but could be changed via user input anytime while the robot was in motion. Left and right heading disturbances were periodically introduced to the system by overriding the iterative procedure enumerated above,

and instead commanding a steady right or left turn for a duration of 1 second.

5.1.5 Results

Nine tests were performed in order to show the real time performance of a vehicle using atmospheric scattering patterns for navigation. During each test, the robot was presented with a series of left and right disturbances, desired heading changes, or a combination of both. Real time heading estimates were computed using the spline interpolation method, the non-linear analytical method, and the radial averaging method. However only the estimates from the non-linear analytical method were used in the control loop. Figure 5.5 shows a comparison of the computed atmospheric based headings to each other and to the results of the determined magnetic heading. In this particular test, the robot is initialized going approximately 0° (north). Then a series of right and left disturbances are introduces, followed by a command to change heading to 90° (east), and then back to 0°.

In order to determine how well the various heading determination methods agreed with each other, a covariance matrix, Σ, was computed between the different methods for each test. Here, Σ is the 4×4 matrix of sample covariances between the two vectors, $\boldsymbol{\psi}_i$ and $\boldsymbol{\psi}_j$, of N heading estimates. Each entry, $\sigma(\boldsymbol{\psi}_i, \boldsymbol{\psi}_j)$, of the covariance matrix is defined as

$$\Sigma(i,j) = \sigma(\boldsymbol{\psi}_i, \boldsymbol{\psi}_j) = \frac{1}{N-1} \sum_{k=1}^{N} \text{circdist}(\boldsymbol{\psi}_i[k] - \bar{\psi}_i)\text{circdist}(\boldsymbol{\psi}_j[k] - \bar{\psi}_j)$$

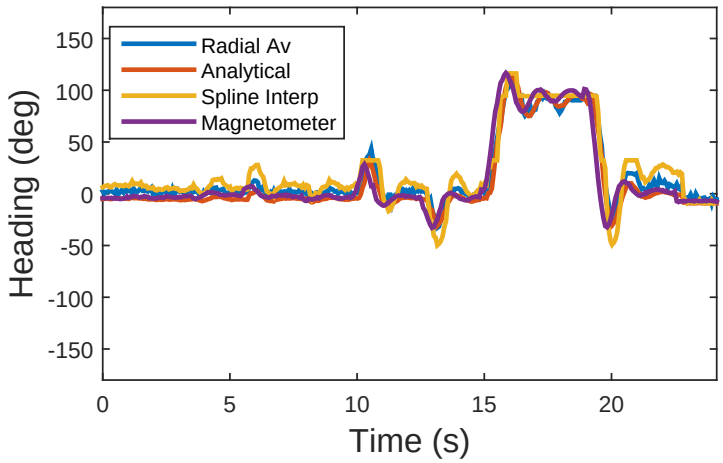

Figure 5.5: Comparison of heading determination methods

where $\bar{\psi}_i$ is the average heading estimate for the N observations using method i. The circdist() function accounts for the fact that heading angles are 360° periodic, and is used to determine the shortest circular distance between to angles. It was observed that there was approximately a 0.227 second lag between the magnetic heading measurements and the atmospheric scattering based methods. Since all of the atmospheric based methods lined up quite closely, it is supposed that the 0.227 second lag is primarily due to webcam image acquisition and buffering time. In order to remove the lag from the correlation analysis, the atmospheric heading measurement vectors were shifted 3 time steps (approximately 0.227 seconds) forward. Σ was then used to compute the correlation coefficient matrix, R, where the entries

$$R(i,j) = \frac{\Sigma(i,j)}{\sqrt{\Sigma(i,i)\Sigma(j,j)}}$$

measure the strength of the linear relationship between heading estimate methods

i and j. The resulting correlation coefficient matrix is presented in Table 5.2.

Table 5.2: Correlation Coefficients

	Radial Av	Analytical	Spline Interp	Magnetometer
Radial Av	1.0000	0.8538	0.8291	0.8160
Analytical	0.8538	1.0000	0.9652	0.9713
Spline Interp	0.8291	0.9652	1.0000	0.9522
Magnetometer	0.8160	0.9713	0.9522	1.0000

Wheel encoder measurements were also used as a method of comparing heading estimates. However, due to frequent failures and delays in reading the serial buffer from the PMS5005, encoder values were not available during the 9 tests presented above. Figure 5.6 presents an earlier test where encoder values were successfully read throughout the entire test. One will notice that while the trend and directionality of the calculated headings from these measurements follows the trend of the other estimates quite well, the magnitude is significantly less. This is likely due to the fact that the parameters computed in section 5.1.3 were based on data from low friction linoleum floors, since the Vicon system could not be brought outdoors. The outdoor concrete surfaces have a significantly higher coefficient of friction. Therefore updated parameter estimates from outdoor data are required to produce more useful heading estimates from encoder measurements.

Figure 5.7 shows the results of a test for which the robot was presented with

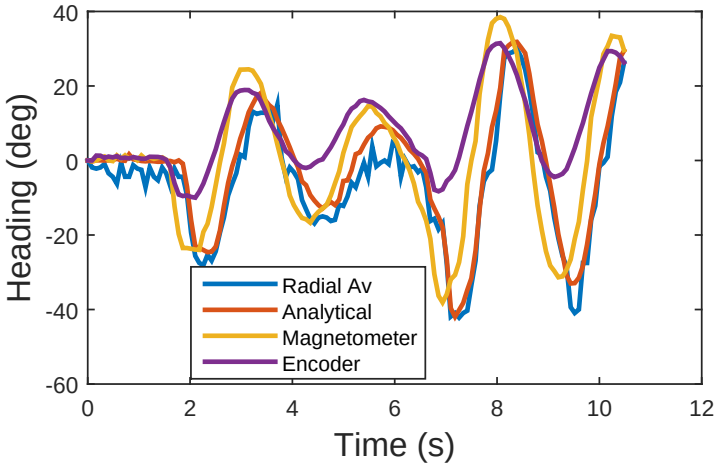

Figure 5.6: Comparison of heading measurements with encoder based heading

a series of right and left disturbances of various amplitudes while being commanded to maintain a heading of approximately $-3°$.

The first four disturbances are about $7°$ disturbances, the fifth disturbance is a $14°$ disturbance, and the last disturbance is a $21°$ disturbance. One will notice that after returning from a response, overshoot is negligible. Settling time is roughly 0.5 seconds for all of the responses. A steady state oscillation of about $1°$ amplitude is maintained likely due to sensor noise and lag.

Figure 5.8 depicts a test for which the robot was commanded to follow a series of different headings. One will observe approximately a $15°$ overshoot after all of these turns, and a settling time of about 2 seconds. Low amplitude steady state oscillations are again observed.

Overall the responses of the system to the PID controller are good. The robot

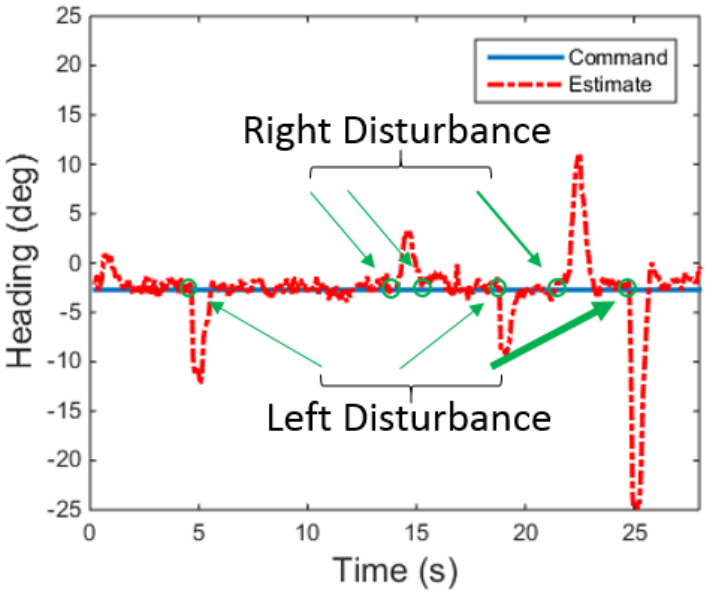

Figure 5.7: Robot response to left and right disturbances

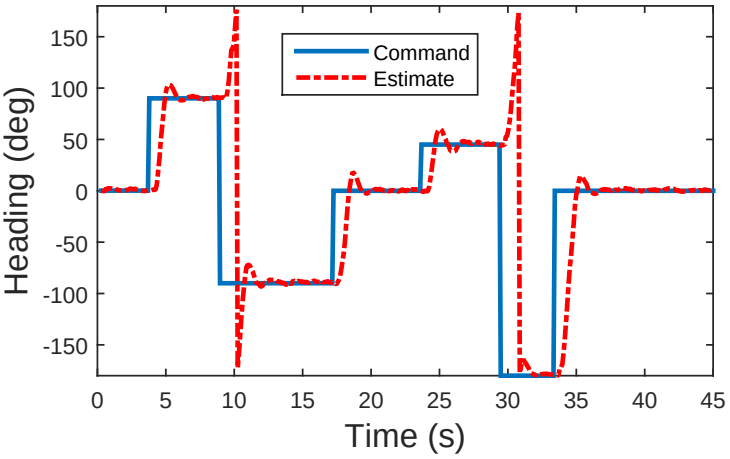

Figure 5.8: Robot response to changes in desired heading

is stabilized to steady state within a relatively short settling time. High overshoot however does indicate that the gains are likely too high. It should be noted that the open loop robot system is *not* stable. When both wheels are commanded equal encoder rate values, the robot has a tendency to drift either left or right, and not to maintain a direction. One will notice that simple PID feedback is able to provide heading stability.

5.2 Quadrotor Simulation

In order to study the feasibility of the developed heading measurement methods on a flight vehicle, a 3D simulation environment was created. This simulation allowed an examination of real-time responses to heading measurements for various camera fields of view and resolution when cameras were not necessarily zenith centered. A realistic quadrotor model was obtained using Peter Corke's Robotic Control Toolbox [56] for MATLAB® and Simulink®. This chapter provides an overview of the atmospheric simulation environment used for this study, a description of the portions of the Robotic Control Toolbox employed, and the controller. Results using each of the heading determination techniques are compared to results from pure state feedback.

5.2.1 Quadrotor Model

The robot control toolbox contains a Simulink library including kinematics, dynamics, and graphing tools for various types of robots. A model of an X-4 Flyer

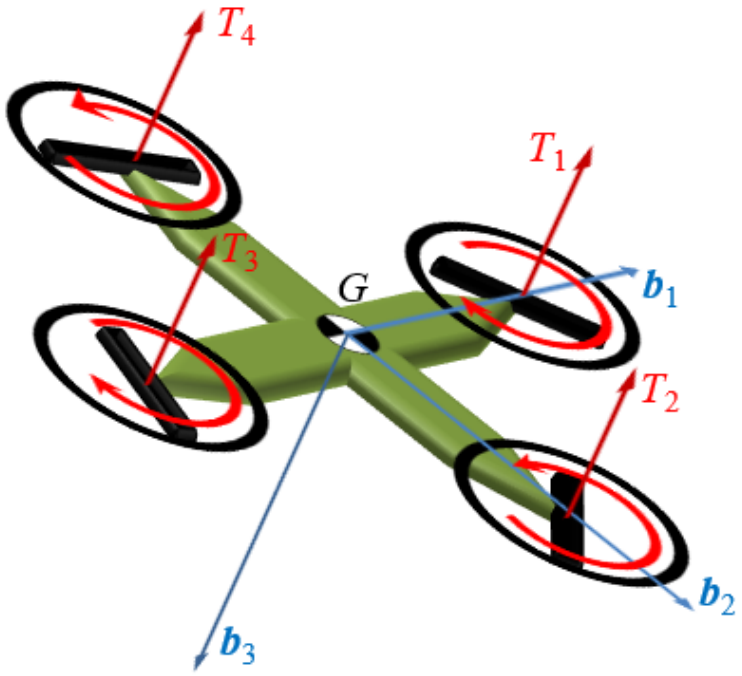

Figure 5.9: Diagram of quadrotor thrusts and and directional conventions

Mark II microquad was chosen for the purposes of this simulation. This model includes dynamics for rotor thrust and flapping, frame aerodynamics, and internal and external motors.

The "quadrotor dynamics" Simulink part takes rotor velocity inputs

$$\mathbf{u} = [\omega_1, \omega_2, \omega_3, \omega_4]$$

corresponding to the front, right, rear, and left rotors with positive directional convention as depicted in Figure 5.9.

The output of the quadrotor model is a vector of the resulting states

$$\mathbf{x} = [x, y, z, \psi, \theta, \phi, u, v, w, r, p, q]^T$$

where $[x, y, z]^T$ are the inertial coordinates of the quadrotor, $[\phi, \theta, \psi]^T$ are the Euler roll pitch and yaw angles corresponding to a 3-2-1 rotation sequence, ${}^{\mathcal{B}}\mathbf{v}_{G/O} = [u, v, w]^T$ are the quadrotor velocities in the body frame, and ${}^{\mathcal{I}}\boldsymbol{\omega}^{\mathcal{B}} = [p, q, r]^T$ are the body angular velocities.

The equations of motion describing a quadrotor's translational dynamics are found by applying Newton's second law to the aircraft center of gravity.

$$\mathbf{F}_G = m{}^{\mathcal{I}}\mathbf{a}_{G/O} = m\frac{{}^{\mathcal{B}}d}{dt}({}^{\mathcal{I}}\mathbf{v}_{G/O}) + {}^{\mathcal{I}}\boldsymbol{\omega}^{\mathcal{B}} \times {}^{\mathcal{I}}\mathbf{v}_{G/O} = mg\mathbf{e}_D - T\mathbf{b}_3 \tag{5.10}$$

In the above equation, aerodynamic lift is assumed negligible, and the applied forces are gravitational force and thrust. Euler's second law can be used to determine the quadrotor's rotational dynamics.

$$\mathbf{M}_G = [\mathcal{I}_G]_{\mathcal{B}} \cdot \frac{{}^{\mathcal{B}}d}{dt}({}^{\mathcal{I}}\boldsymbol{\omega}^{\mathcal{B}}) + {}^{\mathcal{I}}\boldsymbol{\omega}^{\mathcal{B}} \times ([\mathcal{I}_G]_{\mathcal{B}} \cdot {}^{\mathcal{I}}\boldsymbol{\omega}^{\mathcal{B}}) = \sum_{i=1}^{4} \mathbf{r}_{i/G} \times -T_i\mathbf{b}_3 \tag{5.11}$$

The quadrotor is assumed to have bidirectional symmetry, and consequently the moment of inertia matrix, $[\mathcal{I}_G]_{\mathcal{B}}$, is diagonal. Thrust from a single rotor is

$$T_i = b\omega_i^2$$

where, b, the lift constant, is

$$b = C_T \rho A r^2$$

and C_T is the non-dimensional thrust coefficient. The total quadrotor thrust is simply the sum of all the individual rotor thrusts

$$T = b(\omega_1^2 + \omega_2^2 + \omega_3^2 + \omega_4^2). \tag{5.12}$$

To facilitate controller design, a combination of rotor speed inputs can used to define more intuitive inputs directly relating to roll, pitch, yaw, and thrust control.

Letting r be the distance from rotor center to G, the roll and pitch torques are respectively proportional to the following pairwise differences in rotor thrusts

$$\tau_x = rb(\omega_4^2 - \omega_2^2) \tag{5.13}$$

$$\tau_y = rb(\omega_1^2 - \omega_3^2). \tag{5.14}$$

The yaw torque is the sum of the reaction torques of the four rotors, where each reaction torque opposes the direction of rotor rotation.

$$\tau_z = k(\omega_1^2 + \omega_3^2 - \omega_2^2 - \omega_4^2) \tag{5.15}$$

In the above, k is the drag constant where

$$k = C_Q \rho A r^3$$

and C_Q is the non-dimensional torque coefficient.

$$C_Q = C_T\sqrt{C_T/2}.$$

Equations (5.12) through (5.15) can be combined to create a single matrix relationship

$$\begin{pmatrix} T \\ \tau_x \\ \tau_y \\ \tau_z \end{pmatrix} = \begin{pmatrix} -b & -b & -b & -b \\ 0 & rb & 0 & rb \\ rb & 0 & -rb & 0 \\ k & -k & k & -k \end{pmatrix} \begin{pmatrix} \omega_1^2 \\ \omega_2^2 \\ \omega_3^2 \\ \omega_4^2 \end{pmatrix} = M \begin{pmatrix} \omega_1^2 \\ \omega_2^2 \\ \omega_3^2 \\ \omega_4^2 \end{pmatrix}. \tag{5.16}$$

The control mixer part provided by the robot control toolbox uses the inverse of M to generate rotor speed inputs to the quadrotor model based on desired body torques and thrust.

5.2.2 Navigation and control

Insects are able to successfully travel from their home to a food source and back home again. Based on the studies of von Frisch [11] it is very likely that a critical sensory input for foraging bees is polarization vision. This section aims to propose a simple methodology for waypoint navigation using celestial based heading measurements and additional biologically inspired sensing mechanisms. It is then shown how this navigational method can be applied to a quadrotor via nested PD control.

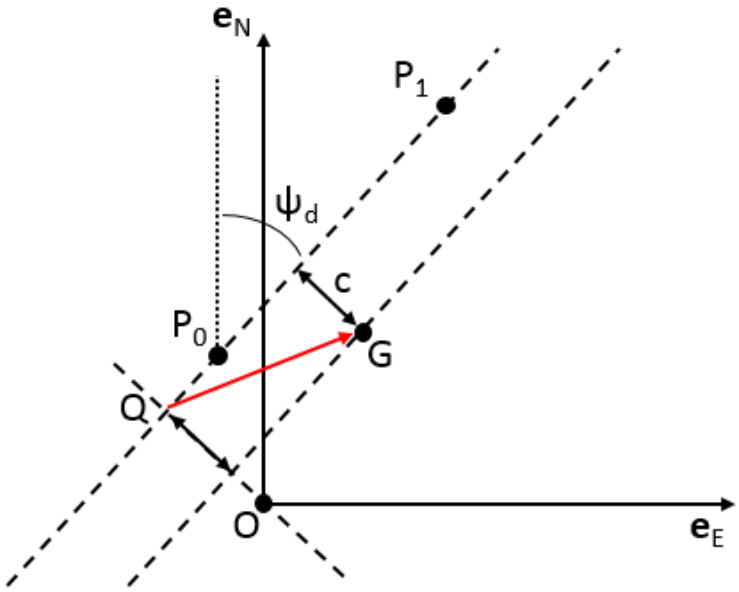

Figure 5.10: Geometry of cross track error

5.2.2.1 Computing Cross and Along Track Errors

The most basic way to travel between two points, P_0 and P_1, on a plane is to maintain a linear trajectory. Since it is assumed that the distances traveled by the quadrotor are relatively short, a flat earth model can be assumed, and a linear trajectory can be used. It is desired that the quadrotor stays as close to the desired trajectory as possible. The distance that the quadrotor is from the desired path is called the cross track error, Δc. In this flat earth scenario, cross track error can be defined as the distance between the center of gravity of the quadrotor, G, and the line defined by the points P_0 and P_1 as shown in Figure 5.10.

To determine the distance between G and the vector from P_0 to P_1, $\mathbf{r}_{P_1/P_0}$, a line through G parallel to $\mathbf{r}_{P_1/P_0}$ is drawn. Next a vector perpendicular to $\mathbf{r}_{P_1/P_0}$ that

intersects the inertial origin O is drawn. The intersection between this perpendicular vector and a line coincident with $\mathbf{r}_{P_1/P_0}$ will be called point Q, and consequently the perpendicular vector will be called $\mathbf{r}_{Q/O}$. If one were then to draw a vector from Q to G, $\mathbf{r}_{G/Q}$, the scalar projection of $\mathbf{r}_{G/Q}$ onto $\mathbf{r}_{Q/O}$ is equivalent to the distance Δc.

$$proj_{\mathbf{r}_{O/Q}}\mathbf{r}_{G/Q} = \frac{\mathbf{r}_{O/Q} \cdot \mathbf{r}_{G/Q}}{|\mathbf{r}_{O/Q}|} = \Delta c \tag{5.17}$$

Solving for (5.17) requires knowledge of the position of Q which can be determined as follows. The equation for the line passing through P_0 and P_1 can be written in terms of slope intercept form as

$$y = mx + b \tag{5.18}$$

where x is the distance north relative to the origin O of some inertial NED frame, y is distance east of O, m is the slope of the line, and b is the y-intercept. Letting $P_0 = x_0\mathbf{e}_N + y_0\mathbf{e}_E$ and $P_1 = x_1\mathbf{e}_N + y_1\mathbf{e}_E$, then

$$m = \frac{y_1 - y_0}{x_1 - x_0}$$

and

$$b = y_0 - mx_0.$$

The equation for the line passing through Q and O will have a slope of $\frac{-1}{m}$, and a

y-intercept of 0.

$$y = \frac{-1}{m}x \tag{5.19}$$

Q is defined as the location where (x, y) is equivalent for (5.18) and (5.19). Consequently

$$\mathbf{r}_{Q/O} = \frac{-mb}{m^2+1}\mathbf{e}_N + \frac{b}{m^2+1}\mathbf{e}_E.$$

Now $\mathbf{r}_{G/Q} = \mathbf{r}_{G/O} - \mathbf{r}_{Q/O}$, where $\mathbf{r}_{G/O} = x_2\mathbf{e}_N + y_2\mathbf{e}_E$. And therefore,

$$\mathbf{r}_{Q/G} = (x_2 + \frac{mb}{m^2+1})\mathbf{e}_N + (y_2 - \frac{b}{m^2+1})\mathbf{e}_E.$$

Solving for (5.17) and simplifying, we get that

$$\Delta c = \frac{-mx_2 + y_2 - b}{\sqrt{m^2+1}}. \tag{5.20}$$

Along track error, Δa, is a measure of the distance along $\mathbf{r}_{P_1/P_0}$ between the vehicle and the next waypoint, P_1. Hence along track error is simply

$$\Delta a = proj_{\mathbf{r}_{P_0/P_1}}\mathbf{r}_{G/P_1} = \frac{\mathbf{r}_{P_0/P_1} \cdot \mathbf{r}_{G/P_1}}{|\mathbf{r}_{P_0/P_1}|} \tag{5.21}$$

where $\mathbf{r}_{G/P_1} = (x_2 - x_1)\mathbf{e}_N + (y_2 - y_1)\mathbf{e}_E$ and $\mathbf{r}_{P_0/P_1} = (x_0 - x_1)\mathbf{e}_N + (y_0 - y_1)\mathbf{e}_E$. Therefore

$$\Delta a = \frac{(x_0 - x_1)(x_2 - x_1) + (y_0 - y_1)(y_2 - y_1)}{\sqrt{(x_0 - x_1)^2 + (y_0 - y_1)^2}} \tag{5.22}$$

is the distance left along the track until the next waypoint is reached.

5.2.2.2 Waypoint Tracking and Control

Insects have been known to reliably travel from their homes to a known food source and back again. As discussed above, evidence suggests the use of atmospheric patterns for insect heading determination. Navigation between two waypoints does not necessarily require a measure of distance traveled. Loizou and Kumar [57] propose a method of navigation in the proximity of 3 landmarks with known relative bearing. While this method is likely quite useful when multiple celestial objects, such as the night stars, are tracked, the sun is the only daytime celestial landmark. Therefore, some measure of distance is needed for daytime navigation using solar heading. Collett et al. [58] suggest that flying insects likely rely on ventral optic flow to approximate distance traveled.

Optic flow describes the patterns of relative motion of objects observed by the visual system of a moving object. More specifically, it is the projection of the velocity vector field of points in the observed environment onto the imaging surface. Therefore the relationship between optic flow and inertial velocity depends on the physical shape of imaging surface. Sabiron et al. [59] and Dev et al. [60] discuss the framework for 2D optic flow projected onto a planar surface, while Hyslop and Humbert [61] present a spherical optic flow model.

Generally speaking, optic flow will have a translational and a rotational component. The relative motion, $\dot{\mathbf{Q}}$, between a spherical optic flow sensor and an observed

point $\mathbf{r}_{P/G} = p_1\mathbf{b}_1 + p_2\mathbf{b}_2 + p_3\mathbf{b}_3$ is

$$\dot{\mathbf{Q}} = -\frac{1}{d}[\mathbf{v} - \langle \mathbf{v}, \mathbf{r}_{P/G}\rangle \mathbf{r}_{P/G}] - \boldsymbol{\omega} \times \mathbf{r}_{P/G} \tag{5.23}$$

where $\mathbf{v} = [u, v, w]^T$ is the body translational velocity, and $\boldsymbol{\omega} = [p, q, r]$ is the body rotational velocity. d is the distance between P and the vehicle along the line from P to the center of the imaging sphere, passing through the projection of P onto the imaging sphere. From (5.23) one can see that in order to directly back out traveled distances, the distance to the observed point is needed. If it is assumed that the environment is relatively flat, a single point measurement such as sonar can be used to obtain d. Additionally pitch and roll rates can be extracted from a biologically inspired ocelli sensor such as proposed by Gremillion et al. [62].

Assuming we have a biologically inspired sensor package consisting of the ASU, ocelli sensors, a ventral optic flow sensor and a sonar sensor kept level to the horizon with a gimbal, estimates of the states ψ, p, r, z, u, and v will be available. Alternately, if the entire sensor suite is not available, but system identification has provided a vehicle dynamic model, a state observer can be designed in order to approximate vehicle states based on measured inputs and outputs of the system.

The along and cross track errors, discussed above, can be used as inputs to control a quadrotor such as the one described in Section 5.2.1. Following controller structure proposed by Peter Corke [56], the roll and pitch torque inputs can be

computed as follows

$$\begin{bmatrix} \tau_y \\ \\ \tau_x \end{bmatrix} = K_{P,2}\left(\left(K_{P,1}\left(R_3(\psi-\psi_d)\begin{bmatrix} \Delta a \\ \\ \Delta c \end{bmatrix} - K_{D,1}\begin{bmatrix} u \\ \\ v \end{bmatrix}\right) - \begin{bmatrix} \theta \\ \\ \phi \end{bmatrix}\right) - K_{D,2}\begin{bmatrix} q \\ \\ r \end{bmatrix}\right) \tag{5.24}$$

where R_3 is the Euler rotation matrix about the inertial 3-axis. Desired heading is computed as

$$\psi_d = \text{atan2}(y_{TO} - y_{FROM}, x_{TO} - x_{FROM})$$

where (x_{TO}, y_{TO}) is the inertial position of the current TO waypoint, and (x_{FROM}, y_{FROM}) is the inertial position of the current FROM waypoint. The current aircraft position in inertial coordinates relative to initial position can then be approximated as follows

$$x_2[t_i] = u[t_i]\cos(\psi[t_i]) - v[t_i]\sin(\psi[t_i]) + x_2[t_{i-1}] \tag{5.25a}$$

$$y_2[t_i] = u[t_i]\sin(\psi[t_i]) + v[t_i]\cos(\psi[t_i]) + y_2[t_{i-1}] \tag{5.25b}$$

assuming small aircraft pitch and roll angles where $\mathbf{r}_{G/O} = x_2\mathbf{e}_N + y_2\mathbf{e}_E$. Quadrotor yaw is commanded via a PD controller of the following form.

$$\tau_z = K_{P,3}(\psi - \psi_d) + K_{D,3}\dot{\psi} \tag{5.26}$$

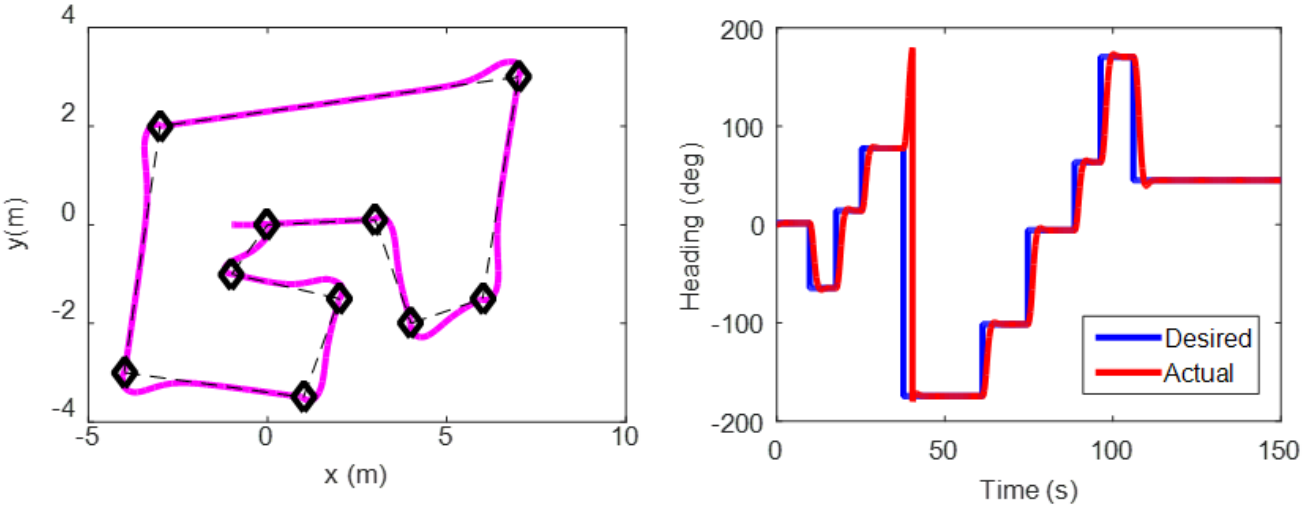

Figure 5.11: Quadrotor Results

Aircraft thrust control is provided by the model feedforward design discussed in [56].

5.2.2.3 Quadrotor Results

Using the methodology discussed above, the quadrotor simulation was provided a counterclockwise trajectory consisting of 10 waypoints shown in Figure 5.11. The quadrotor was commanded to proceed forward towards the next waypoint while maintaining heading such that body x-axis pointed along the direction between the TO and FROM waypoints. The controller described in (5.24) was used to bring the quadrotor to within 0.1 m of the TO waypoint before proceeding to the next waypoint. The integral of measured body velocities was used to approximate inertial distances traveled as describe in (5.25).

Figure 5.11 shows the qualitative performance of the quadrotor. In the first figure, the diamonds depict the waypoints, the dashed line depicts the desired tra-

jectory, and the purple sold line shows the actual trajectory. One will observe that the quadrotor successfully traveled through the desired waypoints and mostly maintained the desired trajectory. The second figure shows the desired heading for the quadrotor (in blue) as a function of time, and the actual quadrotor heading (in red). One will note that the quadrotor appeared to track the desired heading quite well. This initial real time quadrotor simulation test indicates that implementation of a biological sensor package on a physical quadrotor for navigation is certainly feasible.

Chapter 6: Conclusions and Future Work

This thesis provides a methodology for determining solar relative heading from atmospheric scattering patterns, applicable to micro-air vehicle (MAV) navigation. The techniques introduced here provide a reliable, passive heading determination strategy when magnetic heading is not necessarily available. The anatomical structure of the Dorsal Rim Area (DRA) of the insect eye, as well as behavioral and electrophysiological studies, provide inspiration for the sensing design and algorithm development presented here. A low cost, off-the-shelf based Atmospheric Sensory Unit (ASU), consisting of 3 webcams and linear polarizing filters, modeling the insect DRA was modeled and developed.

Several novel algorithms, based on the patterns of atmospheric polarized and unpolarized radiation, were developed to resolve the outputs of the DRA into solar relative heading measurements. Algorithms, based on purely linear computations, are formulated in order to assist future analogue sensor implementations. Additionally, the algorithms presented here can readily be generalized to various sensing schemes including: any polarization filter orientations, n-cameras, or a single CMOS/CCD type sensor. This thesis is also the first work to produce a complete simulation of atmospheric scattering in order to model and analyze sensor outputs

and heading algorithms.

The presented heading determination techniques are demonstrated and validated both in simulation and via an outdoor hardware implementation. Real time heading control through these strategies is then exhibited on a terrestrial differential wheeled robot, and through simulation of a micro-quadrotor.

Several paths exist for future development of the methodology presented in this paper.

1. While the observed errors in heading estimation for the methods developed in this paper are roughly on par with those observed from insect behavioral studies [12] [17], increased heading accuracy is desirable in many scenarios. There are several ways in which estimate accuracy can be improved. The most straightforward of these is to increase the number of pixels per each camera as suggested by Table 4.2. This would increase the resolution of the radial averaging method, and would decrease the effect of each individual pixel. Alternately one could increase the number of cameras and filter angles utilized, which would have the additional result of increasing available knots for the spline interpolation method. Error is also present due to the lack of geometric and intensity calibration between the cameras as discussed in section 4.2.2, and the inability to disable the autofocus feature on the proposed webcams.

   Another source of error present in the proposed hardware implementation is sensor noise. A slight steady state oscillation in heading measurements was observed while the ASU remained stationary. A simple low pass filter could

be implemented on sensor outputs to reduce this noise, or a higher quality and less noisy image sensor could be used instead of the proposed webcams.

2. While the sensing/algorithm set produced heading measurements at a fast enough rate for closed loop control of a ground vehicle, a more efficient methodology might be required for faster moving vehicles, or vehicles with less computational power. As observed in section 5.1.5, an 0.227 second average lag was observed between magnetometer and camera based heading measurements, whereas the delay between visual based heading measurements was negligible. This implies that image acquisition, rather than algorithm computation, is the main source of measurement lag. Image acquisition time can be reduced by decreasing image size, however this has the consequence of reducing estimate accuracy. Alternate hardware is likely a better solution. It is well known that USB transfer rate is rather slow, and that the use of multiple USB devices on a single computer just aggravates the situation. One possibility would be the use of a single integrated vision chip. However this would require development.

3. The presented methodology is somewhat able to compensate for the presence of small clouds by taking the average pixel value over a wide field of view. Better resilience to clouds can be achieved by making use of the UV wavelength rather than visible light as discussed in section 4.2.3. Alternately cloud pixels can be filtered out by removing "white" pixels or following one of the strategies suggested in the introduction to section 3.1.

4. It is likely that in addition to azimuth information, elevation information can

also be reaped from the spatial pattern of atmospheric scattering. One way to do this would be by performing a method similar to the radial averaging method. Once the orientation of the radius containing the highest average intensity is established, a series of lines (or curves if the imaging surface is curved) parallel to the selected radius can be defined. Each of these lines will correspond to an elevation angle, and the line with the highest average intensity will correspond to the solar elevation. Further studies into the spatial pattern of polarized light might reveal additional ways to determine solar elevation.

5. The methods presented here have been used to control a quadrotor in simulation, but not a physical flying vehicle. Implementation of the proposed sensing techniques for real time navigation of a small flight vehicle is a desirable future result. A further achievement would be to develop a biological sensing suite consisting of the ASU, optic flow sensors, and ocelli sensors. The ocelli would provide inner loop pitch and roll stability as well as rate measurements, the optic flow sensors would provide obstacle avoidance capabilities and inertial velocity estimates, and the ASU would provide outer loop heading control and path integration.

6. Many animals such as the nocturnal bee [63] have been shown to use the atmospheric scattering pattern of the night sky for navigation. Expanding the ASU's capability to the dark hours would be a highly beneficial future task.

Appendix A: Reference Frames

Throughout the course of this paper, several different reference frames and coordinates systems are utilized. The purpose of this section is to define the various reference frames, their relationship to each other, and the coordinates used in each reference frame. A reference frame [64] is a "point of view from which observations and measurements are made regarding the motion of a system." Whereas a coordinate system "is the set of scalars that locate the position of a point relative to another point in a reference frame." All reference frames in this paper are defined by 3 perpendicular unit vectors and their shared origin. Rotations will generally be defined as positive when counter-clockwise about a given axis.

Motion of the ground robot is assumed to be planar, thus rotational motion is constrained to yawing or changes in heading. However it is assumed that a MAV can rotate about any of its 3 body axes. It should be recalled here that translational motions of a ground based robot or a MAV are considered negligible when compared to the distance to celestial objects such as the sun and points in the sky. Therefore, when determining heading from atmospheric scattering patterns, it is assumed that at all reference frames have no translational motion relative to one another, but are free to rotate. In this context one can say that vehicle center

of gravity G is approximately equal to some fixed inertial origin O. For vehicle control purpose, this assumption obviously cannot be made. Therefore body fixed translational coordinate frames will be presented with origin G to remain general.

The default inertial[1] reference frame throughout this thesis, $\mathcal{I}_{NED}$, is an earth fixed North-East-Down frame with origin, O, at some fixed latitude and longitude.

$$\mathcal{I}_{NED} = (O, \mathbf{e}_N, \mathbf{e}_E, \mathbf{e}_D)$$

The 1-vector points north, the 2-vector points east, and the 3-vector points down into the earth.

The sun frame, $\mathcal{S}$, is a reference frame whose 1-axis is always along $\mathbf{r}_{S/O}$.

$$\mathcal{S} = (O, \mathbf{s}_1, \mathbf{s}_2, \mathbf{s}_3)$$

The to get from the inertial NED frame to the sun frame, a rotation of ψ_s about the 3-axis followed by a rotation of θ_s about the 2-axis is performed.

The vehicle body frame, $\mathcal{B}$, has its origin at the center of gravity, G.

$$\mathcal{B} = (G, \mathbf{b}_1, \mathbf{b}_2, \mathbf{b}_3)$$

[1]The term inertial here is used loosely. Generally an inertial references frame remains "fixed" in time and space. Newtonian relativity allows this frame to translate constantly without rotation. Since the earth rotates and nutates about the sun, an earth fixed frame is not a true inertial frame. However, since the rotational motions of interest here are those relative to the earth, it is useful to choose an earth fixed frame as an "inertial" frame.

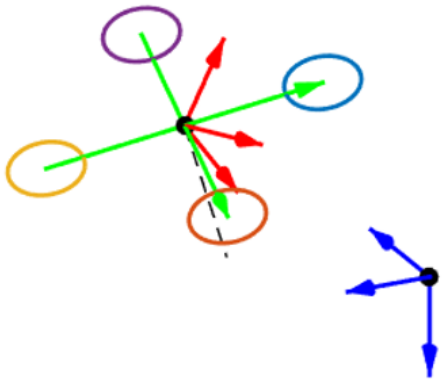

Figure A.1: Inertial NED reference frame (blue), quadrotor and body frame B (green), and Observer frame C (red) fixed to B

For a ground robot, the 1-vector of the body frame point in the direction of forward motion. For a quadrotor, the 1-vector points in the direction of the "front" rotor of the quadrotor. In Figure A.1 the body frame 1 and 2-axes of the quadrotor are depicted by the green arrows attached to the airframe body. The body 3-axis is represented by the downward facing dotted black line. The moving aircraft frame is show relative to the blue NED inertial frame. The 3-2-1 Euler rotation sequence $(\psi_B, \theta_B, \phi_B)$ is used to get from inertial to aircraft body frame.

The observer frame, $\mathcal{C}$, defines a point observed by the sensor relative to the vehicle body frame. The observer frame is fixed to the center of gravity, G. As shown in Figure A.2 A rotation of ψ_c about $\mathbf{b}_3$ followed by a rotation of θ_c about $\mathbf{b}_2$ is used to get from the body frame to the vehicle fixed observer frame. The observer

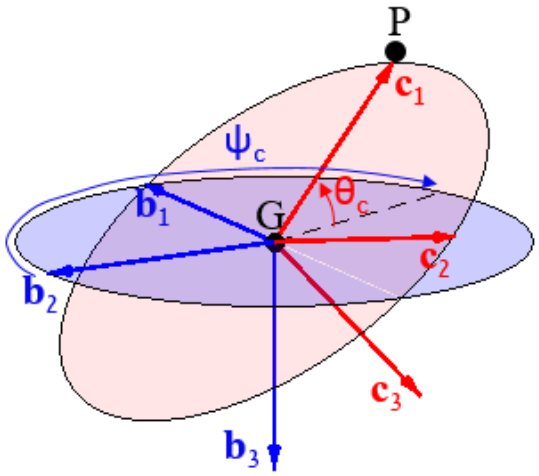

Figure A.2: Body frame (blue) and vehicle fixed observer frame (red)

frame fixed to the aircraft body frame is shown in Figure A.1.

$$\mathcal{C} = (G, \mathbf{c}_1, \mathbf{c}_2, \mathbf{c}_3)$$

The image "figure" frame $\mathcal{F}$ describes the points in the sky in pixel coordinates that an upward facing camera attached to a vehicle would observe. The origin, F is defined as the top left corner of the image. The 1-axis of the image frame is aligned with $-\mathbf{b}_2$, the 2-axis of the image frame is aligned with $-\mathbf{b}_1$, and the 3-axis is aligned with $-\mathbf{b}_3$.

$$\mathcal{F} = (x\mathbf{f}_1, y\mathbf{f}_2, 0\mathbf{f}_3)$$

The vector from the image origin to the aircraft center of gravity can be defined

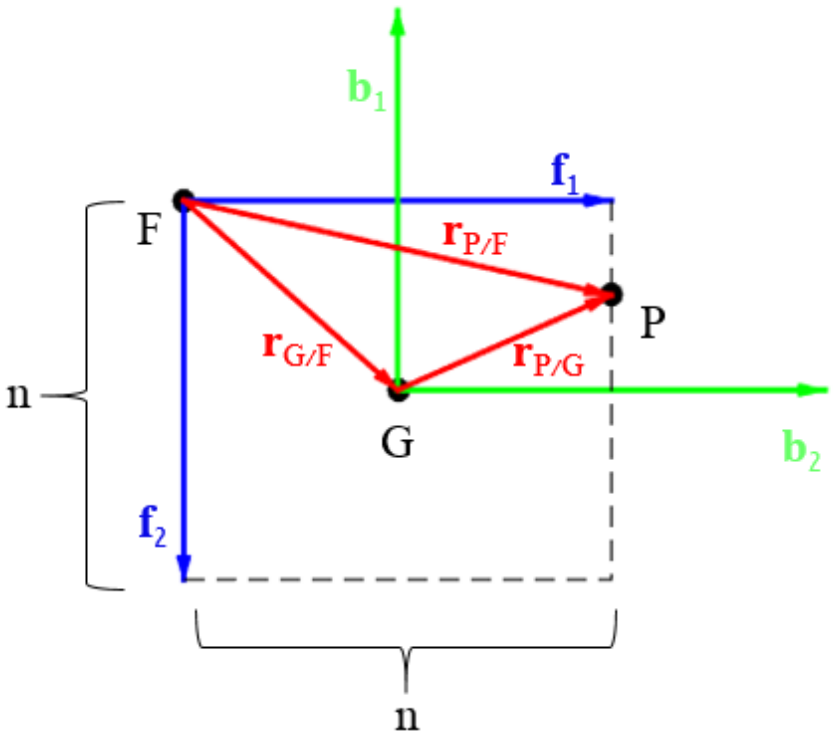

Figure A.3: Image figure frame, $\mathcal{F}$, (blue), Body frame B (green), and Observed point, P

as follows.

$$\mathbf{r}_{G/F} = \frac{n}{2}\mathbf{f}_1 + \frac{n}{2}\mathbf{f}_2$$

where it is assumed that the the image is square, and n is the image side length.

Figure A.3 shows the relationship between the $\mathcal{F}$ and $\mathcal{B}$ frames as well as the vector describing the observed point P in each of these frames. Using some basic vector arithmetic, one can determine the location of point P in the body frame using

the following equality.

$$\mathbf{r}_{P/G} = (\frac{n}{2} - y)\mathbf{b}_1 + (\frac{n}{2} - x)\mathbf{b}_2 + R\mathbf{b}_3$$

Bibliography

[1] Christine Merlin, Stanley Heinze, and Steven M Reppert. Unraveling navigational strategies in migratory insects. *Current opinion in neurobiology*, 22(2):353–361, 2012.

[2] Thomas Labhart and Eric P Meyer. Neural mechanisms in insect navigation: polarization compass and odometer. *Current opinion in neurobiology*, 12(6):707–714, 2002.

[3] Uwe Homberg, Stanley Heinze, Keram Pfeiffer, Michiyo Kinoshita, and Basil El Jundi. Central neural coding of sky polarization in insects. *Philosophical Transactions of the Royal Society B: Biological Sciences*, 366(1565):680–687, 2011.

[4] Rachel Muheim. Behavioural and physiological mechanisms of polarized light sensitivity in birds. *Philosophical Transactions of the Royal Society B: Biological Sciences*, 366(1565):763–771, 2011.

[5] MP Rowe, N Engheta, SS Easter, and EN Pugh. Graded-index model of a fish double cone exhibits differential polarization sensitivity. *JOSA A*, 11(1):55–70, 1994.

[6] Rüdiger Wehner. Polarization vision–a uniform sensory capacity? *Journal of Experimental Biology*, 204(14):2589–2596, 2001.

[7] Stefan Greif, Ivailo Borissov, Yossi Yovel, and Richard A Holland. A functional role of the skys polarization pattern for orientation in the greater mouse-eared bat. *Nature communications*, 5, 2014.

[8] Steven M Reppert. The ancestral circadian clock of monarch butterflies: role in time-compensated sun compass orientation. In *Cold Spring Harbor symposia on quantitative biology*, volume 72, pages 113–118. Cold Spring Harbor Laboratory Press, 2007.

[9] Christine Merlin, Robert J Gegear, and Steven M Reppert. Antennal circadian clocks coordinate sun compass orientation in migratory monarch butterflies. *Science*, 325(5948):1700–1704, 2009.

[10] Karl Von Frisch. *Bees: their vision, chemical senses, and language.* Cornell University Press, 1950.

[11] Karl Von Frisch. *The dance language and orientation of bees.* Harvard University Press, 1967.

[12] Rüdiger Wehner and Martin Müller. The significance of direct sunlight and polarized skylight in the ants celestial system of navigation. *Proceedings of the National Academy of Sciences*, 103(33):12575–12579, 2006.

[13] Samuel Rossel and Rüdiger Wehner. The bee's map of the e-vector pattern in the sky. *Proceedings of the National Academy of Sciences*, 79(14):4451–4455, 1982.

[14] P Kraft, C Evangelista, Marie Dacke, T Labhart, and MV Srinivasan. Honeybee navigation: following routes using polarized-light cues. *Philosophical Transactions of the Royal Society B: Biological Sciences*, 366(1565):703–708, 2011.

[15] T Labhart. How polarization-sensitive interneurones of crickets perform at low degrees of polarization. *Journal of experimental biology*, 199(7):1467–1475, 1996.

[16] Martin Müller and Rüdiger Wehner. Wind and sky as compass cues in desert ant navigation. *Naturwissenschaften*, 94(7):589–594, 2007.

[17] Martina Mappes. Polarization vision: Behavioral studies in tethered flying desert locusts, schistocerca gregaria.

[18] Steven M Reppert, Haisun Zhu, and Richard H White. Polarized light helps monarch butterflies navigate. *Current Biology*, 14(2):155–158, 2004.

[19] Stanley Heinze and Steven M Reppert. Sun compass integration of skylight cues in migratory monarch butterflies. *Neuron*, 69(2):345–358, 2011.

[20] Steven M Reppert, Robert J Gegear, and Christine Merlin. Navigational mechanisms of migrating monarch butterflies. *Trends in neurosciences*, 33(9):399–406, 2010.

[21] M Blum and T Labhart. Photoreceptor visual fields, ommatidial array, and receptor axon projections in the polarisation-sensitive dorsal rim area of the cricket compound eye. *Journal of Comparative Physiology A*, 186(2):119–128, 2000.

[22] Uwe Homberg and Agnes Paech. Ultrastructure and orientation of ommatidia in the dorsal rim area of the locust compound eye. *Arthropod Structure & Development*, 30(4):271–280, 2002.

[23] Thomas Labhart. Polarization-opponent interneurons in the insect visual system. *Nature*, 331(6155):435–437, 1988.

[24] Uwe Homberg. In search of the sky compass in the insect brain. *Naturwissenschaften*, 91(5):199–208, 2004.

[25] Michiyo Kinoshita, Keram Pfeiffer, and Uwe Homberg. Spectral properties of identified polarized-light sensitive interneurons in the brain of the desert locust schistocerca gregaria. *Journal of Experimental Biology*, 210(8):1350–1361, 2007.

[26] Keram Pfeiffer, Michiyo Kinoshita, and Uwe Homberg. Polarization-sensitive and light-sensitive neurons in two parallel pathways passing through the anterior optic tubercle in the locust brain. *Journal of neurophysiology*, 94(6):3903–3915, 2005.

[27] Monika Müller, Uwe Homberg, and Angelika Kühn. Neuroarchitecture of the lower division of the central body in the brain of the locust (schistocerca gregaria). *Cell and tissue research*, 288(1):159–176, 1997.

[28] Stanley Heinze and Uwe Homberg. Neuroarchitecture of the central complex of the desert locust: intrinsic and columnar neurons. *Journal of Comparative Neurology*, 511(4):454–478, 2008.

[29] Stanley Heinze and Uwe Homberg. Maplike representation of celestial e-vector orientations in the brain of an insect. *Science*, 315(5814):995–997, 2007.

[30] Stanley Heinze, Sascha Gotthardt, and Uwe Homberg. Transformation of polarized light information in the central complex of the locust. *The Journal of Neuroscience*, 29(38):11783–11793, 2009.

[31] Ulrike Träger and Uwe Homberg. Polarization-sensitive descending neurons in the locust: Connecting the brain to thoracic ganglia. *The Journal of Neuroscience*, 31(6):2238–2247, 2011.

[32] Midori Sakura, Dimitrios Lambrinos, and Thomas Labhart. Polarized skylight navigation in insects: model and electrophysiology of e-vector coding by neurons in the central complex. *Journal of neurophysiology*, 99(2):667–682, 2008.

[33] Leif K Karlsen. *Secrets of the Viking navigators*. One Earth Press, 2003.

[34] Charles D Campbell. A sky compass for field use. *Northwest Science*, 28:43, 1954.

[35] G Horváth and R Wehner. Skylight polarization as perceived by desert ants and measured by video polarimetry. *Journal of Comparative Physiology A*, 184(1):1–7, 1999.

[36] István Pomozi, Gábor Horváth, and Rüdiger Wehner. How the clear-sky angle of polarization pattern continues underneath clouds: full-sky measurements and implications for animal orientation. *Journal of Experimental Biology*, 204(17):2933–2942, 2001.

[37] Dimitrios Lambrinos, Hiroshi Kobayashi, Rolf Pfeifer, Marinus Maris, Thomas Labhart, and Rüdiger Wehner. An autonomous agent navigating with a polarized light compass. *Adaptive behavior*, 6(1):131–161, 1997.

[38] Dimitrios Lambrinos, Ralf Möller, Thomas Labhart, Rolf Pfeifer, and Rüdiger Wehner. A mobile robot employing insect strategies for navigation. *Robotics and Autonomous systems*, 30(1):39–64, 2000.

[39] Jinkui Chu, Kaichun Zhao, Qiang Zhang, and Tichang Wang. Design of a novel polarization sensor for navigation. In *Mechatronics and Automation, 2007. ICMA 2007. International Conference on*, pages 3161–3166. IEEE, 2007.

[40] Jinkui Chu, Kaichun Zhao, Qiang Zhang, and Tichang Wang. Construction and performance test of a novel polarization sensor for navigation. *Sensors and Actuators A: Physical*, 148(1):75–82, 2008.

[41] Kaichun Zhao, Jinkui Chu, Tichang Wang, and Qiang Zhang. A novel angle algorithm of polarization sensor for navigation. *Instrumentation and Measurement, IEEE Transactions on*, 58(8):2791–2796, 2009.

[42] Yoshiyuki HIGASHI, Hiroaki TOKUAMI, and Hiroshi KIMURA. Robot navigation using polarized light sensor without crossed-analyzer. In *Proc. of 6th Int. Symp. on Advanced Science and Technology in Experimental Mechanics*, volume 110, 2011.

[43] Daobin Wang, Huawei Liang, Hui Zhu, and Shuai Zhang. A bionic camera-based polarization navigation sensor. *Sensors*, 14(7):13006–13023, 2014.

[44] Mukul Sarkar, David San Segundo Bello, Chris Van Hoof, and Albert Theuwissen. Integrated polarization analyzing cmos image sensor for autonomus navigation using polarized light. In *Intelligent Systems (IS), 2010 5th IEEE International Conference*, pages 224–229. IEEE, 2010.

[45] Kinsell L Coulson. *Polarization and Intensity of Light in the Atmosphere*. A. Deepak Pub., 1988.

[46] Earl J McCartney. *Optics of the atmosphere: scattering by molecules and particles*. New York, John Wiley and Sons, Inc., 1976.

[47] Ivo Sauman, Adriana D Briscoe, Haisun Zhu, Dingding Shi, Oren Froy, Julia Stalleicken, Quan Yuan, Amy Casselman, and Steven M Reppert. Connecting the navigational clock to sun compass input in monarch butterfly brain. *Neuron*, 46(3):457–467, 2005.

[48] Basil El Jundi and Uwe Homberg. Evidence for the possible existence of a second polarization-vision pathway in the locust brain. *Journal of insect physiology*, 56(8):971–979, 2010.

[49] David D Lent, Paul Graham, and Thomas S Collett. Image-matching during ant navigation occurs through saccade-like body turns controlled by learned visual features. *Proceedings of the National Academy of Sciences*, 107(37):16348–16353, 2010.

[50] Keram Pfeiffer and Uwe Homberg. Coding of azimuthal directions via time-compensated combination of celestial compass cues. *Current biology*, 17(11):960–965, 2007.

[51] Boris I Kvasov and Boris I Kvasoc. *Methods of shape-preserving spline approximation*. World Scientific, 2000.

[52] http://www.psa.es/sdg/sunpos.htm. *PSA Algorithm Files*.

[53] Christopher Cornwall, A Horiuchi, and C Lehman. Noaa esrl solar position calculator, 2007.

[54] Walter Gander, Gene H Golub, and Rolf Strebel. Least-squares fitting of circles and ellipses. *BIT Numerical Mathematics*, 34(4):558–578, 1994.

[55] Vladislav Klein and Eugene A Morelli. *Aircraft system identification: theory and practice*. American Institute of Aeronautics and Astronautics Reston, VA, USA, 2006.

[56] Peter Corke. *Robotics, vision and control: fundamental algorithms in MATLAB*, volume 73. Springer Science & Business Media, 2011.

[57] Savvas G Loizou and Vijay Kumar. Biologically inspired bearing-only navigation and tracking. In *Decision and Control, 2007 46th IEEE Conference on*, pages 1386–1391. IEEE, 2007.

[58] Matthew Collett, Thomas S Collett, and Mandyam V Srinivasan. Insect navigation: measuring travel distance across ground and through air. *Current biology*, 16(20):R887–R890, 2006.

[59] Guillaume Sabiron, Paul Chavent, Thibaut Raharijaona, Patrick Fabiani, and Franck Ruffier. Low-speed optic-flow sensor onboard an unmanned helicopter flying outside over fields. In *Robotics and Automation (ICRA), 2013 IEEE International Conference on*, pages 1742–1749. IEEE, 2013.

[60] Anuj Dev, Ben Krose, and Frans Groen. Navigation of a mobile robot on the temporal development of the optic flow. In *Intelligent Robots and Systems, 1997. IROS'97., Proceedings of the 1997 IEEE/RSJ International Conference on*, volume 2, pages 558–563. IEEE, 1997.

[61] Andrew M Hyslop and J Sean Humbert. Autonomous navigation in three-dimensional urban environments using wide-field integration of optic flow. *Journal of guidance, control, and dynamics*, 33(1):147–159, 2010.

[62] Gregory Gremillion, J Sean Humbert, and Holger G Krapp. Bio-inspired modeling and implementation of the ocelli visual system of flying insects. *Biological cybernetics*, 108(6):735–746, 2014.

[63] Birgit Greiner, Thomas W Cronin, Willi A Ribi, William T Wcislo, and Eric J Warrant. Anatomical and physiological evidence for polarisation vision in the nocturnal bee megalopta genalis. *Journal of Comparative Physiology A*, 193(6):591–600, 2007.

[64] N Jeremy Kasdin and Derek A Paley. *Engineering dynamics: a comprehensive introduction*. Princeton University Press, 2011.